Noninvasive Submillimeter-Precision Brain Stimulation by Optically-Driven Focused Ultrasound

Yueming Li[1, †], Ying Jiang[2, †, ‡], Lu Lan[3, †], Xiaowei Ge[3], Ran Cheng[4], Yuewei Zhan[5], Linli Shi[4], Nan Zheng[6], Guo Chen[3], Runyu Wang[3], Chen Yang[3,4, *], Ji-Xin Cheng[3,5, *]

[1] Department of Mechanical Engineering, Boston University, Boston, MA 02215, USA.

[2] Graduate Program for Neuroscience, Boston University, Boston, MA 02215, USA.

[3] Department of Electrical and Computer Engineering, Boston University, Boston, MA 02215, USA.

[4] Department of Chemistry, Boston University, Boston, MA 02215, USA.

[5] Department of Biomedical Engineering, Boston University, Boston, MA 02215, USA.

[6] Division of Materials Science and Engineering, Boston University, Boston, MA 02215, USA.

† These authors contributed equally to this work.

‡ Current affiliation: Department of Biological Engineering, Massachusetts Institute of Technology, Cambridge, MA 02142, USA

* Corresponding author. Email: jxcheng@bu.edu (J.C.); cheyang@bu.edu (C.Y.).

Abstract -- High precision neuromodulation is a powerful tool to decipher neurocircuits and treat neurological diseases. Current non-invasive neuromodulation methods offer limited millimeter-level precision. Here, we report an optically-driven focused ultrasound (OFUS) for non-invasive brain stimulation with submillimeter precision. OFUS is generated by a soft optoacoustic pad (SOAP) fabricated through embedding candle soot nanoparticles in a curved polydimethylsiloxane film. SOAP generates a transcranial ultrasound focus at 15 MHz with a lateral resolution of 83 μm, which is two orders of magnitude smaller than that of conventional transcranial focused ultrasound (tFUS). Effective OFUS neurostimulation *in vitro* with a single ultrasound cycle is shown. Submillimeter transcranial stimulation of mouse motor cortex *in vivo* is demonstrated. An acoustic energy of 0.02 J/cm^2, two orders of magnitude less than that of tFUS, is sufficient for successful OFUS neurostimulation. By delivering a submillimeter focus non-invasively, OFUS opens a new way for neuroscience studies and disease treatments.

Keywords – Optoacoustic neuromodulation, noninvasive neuromodulation, ultrasound, sub-millimeter, candle soot, PDMS

1 INTRODUCTION

To understand how brain functions and how its dysfunction causes diseases, modalities to modulate neuronal activity with high precision are needed. In small animals, brain stimulations with millimeter precision usually activate multiple functional regions and cause unintended responses [2]. Such limited precision hinders the mapping of brain function, for example, when responses in multiple body parts were observed during the mapping of the motor cortex in mice [3]. Therefore, a neuromodulation tool with sub-millimeter precision is needed for mapping the brain sub-regions, from the motor cortex to the deep brain, by modulate a small population of neurons [4]. For human, this spatial resolution can provide stimulation volumes corresponding to individual nuclei in thalamus [5]. Electrical stimulation tools have already been a gold standard in neuromodulation studies and disease

treatment. For example, deep brain stimulation with implanted electrodes has been approved for clinical treatments of Parkinson's disease, depression, and epilepsy [6-8]. However, the current spread over several millimeters limits the precise control of targeting in electrical stimulation [9]. Optogenetics provides an unrivaled sub-cellular spatial resolution and specificity in targeted cell types, which has advanced the studies of neuroscience [10-12]. Recently developed transcranial optogenetics in mice can further avoid surgery and successfully stimulate a brain area ~ 0.8 to 1 mm laterally at a penetration depth of 5 ~ 6 mm [13, 14]. However, transcranial optogenetics has a light transmission rate of ~ 0.02% at 7 mm. Therefore, to develop sufficient light energy to a depth of 7 mm and beyond, there is an increased risk of heat accumulation along the light path in the illuminated tissue. Furthermore, both conventional and transcranial optogenetics rely on viral transfection which has yet limited their applications in human brains.

Non-invasive non-genetic neuromodulation is attractive as it avoids the risk of surgery and is applicable to human brains. Transcranial direct current stimulation (tDCS) and transcranial magnetic stimulation (TMS) [15-17] provide a spatial resolution of centimeter-level due to the long wavelength of electromagnetic waves used. The emerging transcranial focused ultrasound (tFUS) as a non-invasive neuromodulation method offers higher precision in various models, such as mouse [18-20], rat [21, 22], rabbits [23], monkey [24], and even in human [25-27]. To achieve high transcranial efficiency, transducer-based tFUS with a low ultrasonic frequency of ~ 1 MHz or less is preferred, which limits its spatial resolution from 1 to 5 millimeters [28]. Non-invasive non-genetic neuromodulation with a submillimeter precision remains a critical unmet need.

The optoacoustic effect is an alternative way to generate ultrasound. Optoacoustic materials absorb a short pulse of light and convert it into a transient temperature increase and thermal expansion and compression, resulting in the generation of an ultrasound pulse [29, 30]. Recently Jiang et al. and Shi et al. reported a fiber-based optoacoustic emitter and tapered fiber optoacoustic emitter for submillimeter and single neuron stimulation, respectively [31-33]. In these fiber optoacoustic emitters, the optoacoustic materials are coated on the tips of optical fibers. The coated fiber tip acts as a point source of ultrasound, providing a resolution from submillimeter to a few tens of microns, enabling a selective activation of subcellular structures. However, since they exploit near-field ultrasound for localized neuromodulation, fiber optoacoustic emitters need to be surgically implanted to the target and can't be applied transcranially.

Here, we report the development of an optically-driven focused ultrasound (OFUS) for non-invasive neuromodulation at submillimeter precision. OFUS is generated by a curved soft optoacoustic pad (SOAP) upon a nanosecond laser excitation. SOAP is fabricated using polydimethylsiloxane (PDMS) and a carbon-based absorber. To enable a tighter spatial focusing and to maximize the focal pressure, the diameter of the curvature was tailored to provide a numerical aperture (NA) of 0.95, which is close to the theoretical limit of 1 and much larger than that of a typical conventional lead zirconate titanate (PZT)-based transducer. To identify the optimal absorber for efficient conversion of photons to acoustic wave, SOAPs based on four different optoacoustic materials, including heat shrink membrane, carbon nanotube mixed with PDMS, carbon nanoparticle mixed with PDMS, and candle soot layered with PDMS (CS-PDMS), were fabricated and tested. Their optoacoustic conversion efficiencies were compared by measuring the pressure at the foci. The CS-PDMS SOAP is found to be the most efficient, generating ~ 48 MPa at the ultrasound focus under 0.62 mJ/cm^2 laser input. We further demonstrate that CS-PDMS OFUS produces a ~ 83 μm spatial resolution with transcranial ability, which is a two orders of magnitude improvement

from the resolution of a few millimeters offered by tFUS. Verified by calcium imaging, we achieved direct and transcranial single-pulse OFUS stimulation reliably and safely in cultured neurons *in vitro*. The total ultrasound energy input of OFUS was found to be two orders of magnitude less than that of conventional transducer when evoking the similar level of neuron responses [1]. OFUS non-invasive transcranial brain stimulation in mice is also demonstrated. Immunofluorescence imaging confirms a stimulation volume of submillimeter in mouse brains. Lastly, we validated the functional outcomes by OFUS stimulation of mouse motor cortex and electrophysiological recording *in vivo*.

2 MAIN CONTENT

2.1 FABRICATION OF SOAP AND OPTIMIZATION OF OPTOACOUSTIC EFFICIENCY

Fig. 1A shows the schematic illustration of SOAP composed of a PDMS substrate and a curved layer of optical absorbers. A nanosecond laser is delivered from the PDMS side. Through the optoacoustic effect, ultrasound waves are generated at the surface of the curved absorber layer. The waves emitted from different angles on the curvature arrive at its geometric center in-phase. A focal distance of 2 mm is designed to ensure that the generated ultrasound can penetrate the mouse skull and reach the cortical layer.

To optimize the geometric design of SOAP, we firstly used numerical simulations to predict generated acoustic fields. Numerical simulations using k-wave toolbox in MATLAB were performed to calculate the generated acoustic field [34]. In a 2D simulation, a block of PDMS with a curvature was placed at the interface of water and air. The corresponding sound speed and density were used, respectively. To model the optoacoustic layer, a single layer of grid on the curvature was assigned as the source of ultrasound. A central frequency of 15 MHz and a bandwidth of 200% were set according to reported photoacoustic frequencies generated by carbon-based absorbers [35, 36]. The generated ultrasound propagated into the water with air-backing to mimic the application scenarios. A focal distance of 2 mm between the ultrasound focus and the top flat surface of SOAP was fixed. Then, we tuned the radius and the curvature diameter of SOAP to obtain the ultrasound field at the focus. The lateral resolution at the focus, defined as the full width at half maximum (FWHM) of the generated ultrasound field at the focus, was obtained from the simulated ultrasound field.

The simulated lateral resolution R as a function of the NA, calculated based on the ratio of the curvature diameter to the radius, is plotted in **Fig. 1B**. The lateral resolution is reversely proportional to the NA, shown in a fitting curve (red) of R = 71.51/NA (R^2 = 0.9899, fitting coefficient of determination). Therefore, a larger NA can provide a better lateral resolution. This relationship agrees with the equation of the lateral resolution in acoustic-resolution photoacoustic microscopy. The lateral resolution depending on the NA follows the equation below[29].

$$R_L = 0.71\frac{v}{NA \cdot f} \quad (1)$$

Here, v is the ambient sound speed, f is the central frequency. The orange area in **Fig. 1B** indicates the range of NA in conventional PZT-based transducers [4, 37-41]. In PZT-based single-element focused ultrasound transducers, it is difficult to reach a high NA due to the cracking in the single crystal piezoelectric material [42]. However, a high NA up to 0.95, close to the theoretical limit value of 1, can be achieved in a soft optoacoustic material. OFUS is expected to deliver a lateral resolution of 75 μm at the focus corresponding to a NA of 0.95. In comparison, a conventional transducer at the same ultrasonic frequency delivers a lateral resolution of 132 μm.

Fig. 1C shows the stimulated results of ultrasound field corresponding to the high NA of 0.95. The radius and the curvature diameter of SOAP are 6.35 mm and 12.1 mm, respectively. The result confirms that this geometry provides a focused ultrasound field at the center of the curvature as expected. The simulated OFUS at

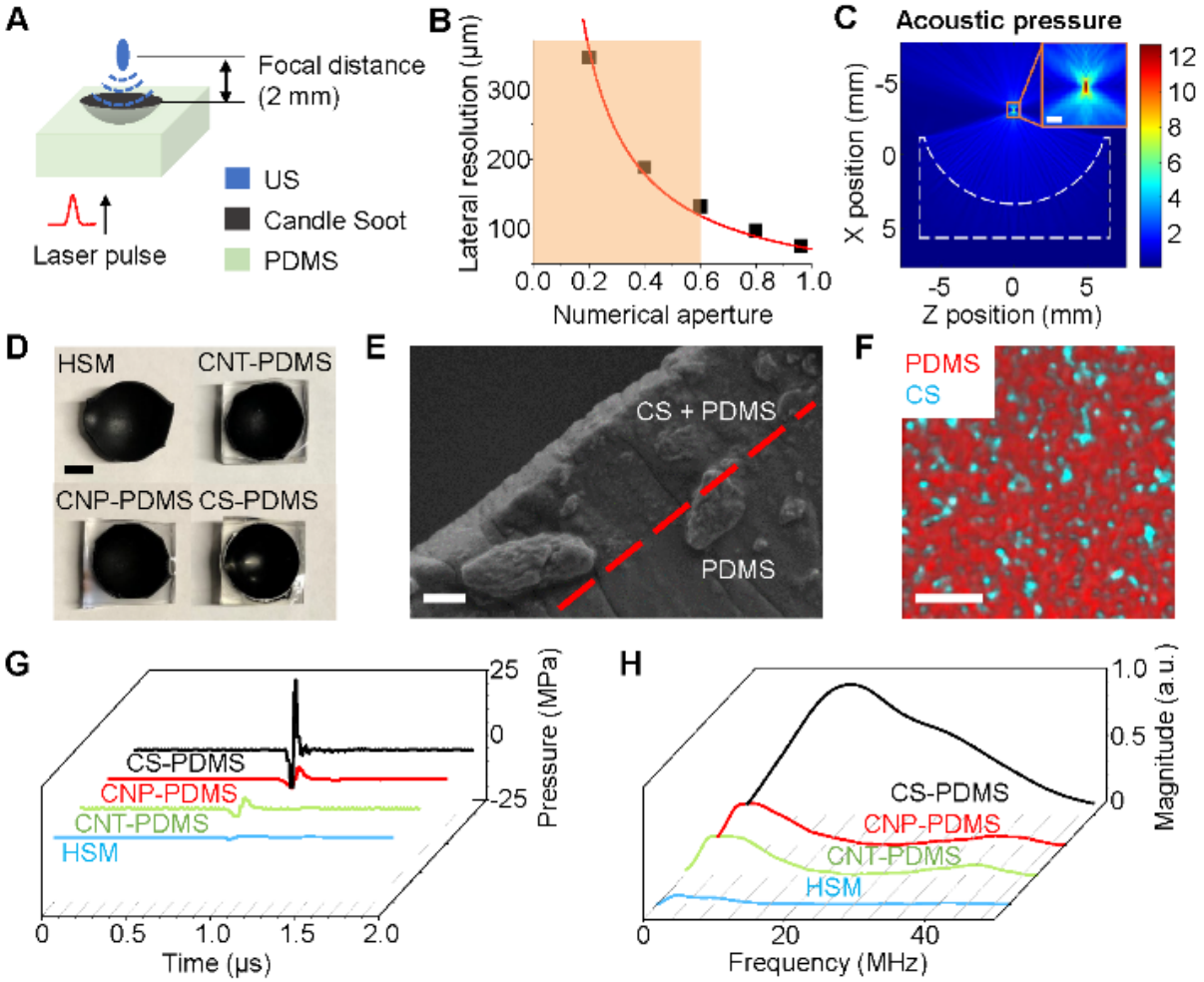

Fig. 1. Design, fabrication, and characterization of SOAP. (**A**) Schematic of SOAP design. (**B**) Numerical aperture and lateral resolution. Red line: fitting curve. Orange area: NA range of conventional ultrasound transducer. (**C**) The acoustic field generated by SOAP in k-wave simulation with designed geometry. Dashed line: the position of SOAP. Inset: zoom in at acoustic focus. Scale bar: 200 μm. (**D**) Photos of 4 kinds of SOAPs with the same geometric design. From left to right, top to bottom: heat shrink membrane (HSM), carbon nanotube-PDMS (CNT-PDMS), carbon nanoparticles-PDMS (CNP-PDMS), candle soot-PDMS (CS-PDMS). Scale bar: 5 mm. (**E**) SEM image of CS-PDMS SOAP cross-section. Dashed red line separated CS and PDMS mixture region and pure PDMS region. Scale bar: 1 μm. (**F**) Spatially distribution of PDMS and CS in the mixture by SRS and photothermal imaging. Red: PDMS. Cyan: CS. Scale bar: 100 nm. (**G**) The ultrasound waveforms from the 4 kinds of SOAPs with the same laser energy input. (**H**) The frequency spectra of ultrasound from the 4 kinds of SOAPs**.**

the focus has a lateral resolution at FWHM of 78 μm, which is consistent with the calculation results above. An axial resolution of 209 μm was obtained (**Fig. S1**). This lateral spatial resolution is sufficient for submillimeter precision neurostimulation in small animals.

Such a high NA provides OFUS not only with a high lateral resolution but also a high focal gain G at the focus. G is defined by the ratio of the pressure at the focal point to the pressure on the spherical surface. A spherical surface with a high

NA corresponding to a low f-number, defined as the ratio of the radius to the curvature diameter,

provides a high focal gain G according to the equation below [43].

$$G = \frac{2\pi f}{c_0} r \left(1 - \sqrt{1 - \frac{1}{4f_N^2}}\right) \quad (2)$$

In this equation, $f, c_0, r,$ and f_N stands for the acoustic frequency, the speed of sound in the medium, the radius of curvature, and the f-number, respectively. Considering the water attenuation coefficient $2.2 \times 10^{-3}\,\mathrm{dB/(cm \times MHz^2)}$ with a 2 mm focal distance and a frequency of 15 MHz, we estimate the effective focal gain $G_{eff} \approx 280$ for SOAP with a f_N of 0.52. This focal gain is 5 fold higher than the focal gain of a conventional PZT-based transducer with f_N of 1, and 92 fold higher than that of a transducer with f_N of 4 [4, 37-41]. In summary, taking advantage of a high NA close to the limit in SOAP, OFUS enables a lateral resolution less than 100 μm at 15 MHz and a focal pressure up to 92 fold compared to a PZT-based transducer at the same frequency.

In addition to the geometry, we also evaluated 4 different absorbers to optimize the optoacoustic conversion efficiency experimentally. We fabricated SOAP with the same geometric design described in **Fig. 1C** based on heat shrink membrane (HSM), carbon nanotube (CNT), carbon nanoparticle (CNP), and candle soot (CS) (**Fig. 1D**). For HSM, the elastic black polyolefin itself serves as the light-absorber and expansion material simultaneously. In the other three designs, the carbon-based materials, as light-absorbers, are embedded in PDMS that serves as the expansion material. **Fig. S2** shows the fabrication method using CS-PDMS as an example. Briefly, a metal ball was coated with candle soot from exposing to candle flame from 10 to 15 s and then dipped into PDMS. This candle soot layer was transferred to PDMS by curing PDMS at 110 °C for 15 min. A CS-PDMS SOAP was obtained by removing the metal ball. The fabrication methods for other SOAPs are described in the Methods.

To investigate whether the transfer process produced a well-mixed matrix of CS and PDMS, we sliced the CS-PDMS SOAP to thin layers with a thickness of ~ 200 μm and examined the morphology using scanning electron microscopy (SEM). A mixed layer composed of PDMS and evenly embedded CS particles can be distinguished from the smooth pure PDMS layer (**Fig. 1E**). The mixture layer has a thickness of 2.7 μm, which is very close to the theoretical thickness of 2.15 μm for the optimal optoacoustic transduction of CS-PDMS [44]. From the SEM image, we identified that the diameter of CS nanoparticles was ~ 55 nm (**Fig. S3)**, which is comparable to the size of CS nanoparticles prepared by the same method reported in the literature [45, 46]. Additionally, the deposition rate of the CS layer estimated from the film thickness was ~ 200 μm/s, consistent with the documented rate [45].

Besides the morphology, chemical composition of the CS-PDMS composite was examined by label-free stimulated Raman scattering (SRS) and photothermal imaging (**Fig. S4**). The femtosecond SRS of C-H bonds in PDMS only occurs when the two beams, a pump and a Stokes laser beam, temporally overlapped (t ~ 0 s), while the candle soot's photothermal signal has a much slower decay, which is close to constant with the delay between two laser beams. Therefore, we can chemically map the spatial distribution of the CS particles in the PDMS by photothermal and SRS imaging of the same sample. The merged image illustrates a uniform matrix of CS and PDMS (**Fig. 1F**). Such a uniform mixture allows for rapid transfer of heat from light-absorbing CS to PDMS, which is a foundation for efficient optoacoustic conversion.

To characterize the optoacoustic efficiency of the four fabricated SOAPs, we delivered a 1064 nm pulsed laser with an 8 ns pulse width and 0.62 mJ/cm^2 laser input to each design to generate OFUS signals. A needle hydrophone was used to record the waveforms and pressure of the optoacoustic signals generated (**Fig. 1G**). The

HSM provides the smallest amplitude, 5 times smaller compared to CNT- and CNP-PDMS. Signals from CNT- and CNP-PDMS are at the same level. CS-PDMS generates ~ 48 MPa, which is 6-fold larger than that of CNT- and CNP-PDMS. This result is consistent with previous reports [45]. The ultrasound pulse widths of HSM, CNT-, CNP-, and CS-PDMS are 0.31 μs, 0.24 μs, 0.29 μs, and 0.09 μs, respectively. The frequency spectrum of the OFUS signals is shown in **Fig. 1H**. The HSM produces a central frequency at ~ 3 MHz, and the CNT- and CNP-PDMS provides a higher central frequency at ~ 5 MHz. The CS-PDMS generates the highest central frequency at ~ 15 MHz. – 6 dB widths were found at 5 and 35 MHz and the ultrasound signal of CS-PDMS has a broad bandwidth of 200%. We selected CS-PDMS for further experiments based on its highest optoacoustic conversion efficiency compared to other SOAPs and its highest central frequency to provide a tight focus. We further characterized the light leakage of CS-PDMS with a power meter. Only 2% of light energy is detected behind CS-PDMS, demonstrating that up to 98% of the light energy is absorbed by CS-PDMS. A linear relation between the input laser pulse energy and CS-PDMS generated OFUS pressure at the focus was also confirmed (**Fig. S5**). In conclusion, we have fabricated a SOAP made of CS-PDMS with a high NA, high focal gain, and high optoacoustic conversion efficiency for neural stimulation.

2.2 OFUS DEMONSTRATES A HIGH SPATIAL RESOLUTION AND TRANSCRANIAL EFFICIENCY

To confirm that OFUS provides a high spatial resolution after penetrating skulls for non-invasive applications, we characterized the resolution of OFUS before and after penetrating a piece of mouse skull. The CS-PDMS SOAP placed in a water tank was illuminated with laser pulses. A needle hydrophone was employed to acquire the ultrasound profile from the top of SOAP (**Fig. 2A**). To test transcranial ability, we placed a piece of mouse skull (thickness ~ 0.15 mm) between the hydrophone and SOAP. The transcranial efficiency of OFUS was evaluated by measuring the amplitude of the transcranial ultrasound signal and normalizing it to the peak amplitude of the signal without the presence of the skull at the focus (**Fig. 2B**). Compared to the one without skull, the transcranial efficiency of OFUS is 69 %. Such a high efficiency is sufficient for future transcranial applications. The frequency spectrum shows that a high central frequency remains after the penetration of the mouse skull (Supplementary **Fig. S6**). This high frequency ensures a high transcranial precision.

To characterize the focus size without and with a mouse skull in the path, we swept the focus to acquire lateral and axial profiles (**Fig. 2C** and **2D**). The hydrophone was mounted to an XYZ translation stage and moved at a step of 12.7 μm to acquire these profiles. All profiles were normalized to the peak amplitude of the signal without the skull for comparison. We define lateral and axial resolution according to the FWHM in the respective directions. The lateral and axial resolutions of OFUS without the presence of the skull are found to be 66 μm and 284 μm, close to simulation data. With the presence of the skull, the FWHMs are 83 μm and 287 μm, respectively, showing no substantial change in the focus size after penetrating through the mouse skull. These resolutions are two orders of magnitude higher than the resolution of low-frequency ultrasound typically used in neuromodulation, which was ~ 5 mm and ~ 40 mm respectively for a 0.5 MHz transducer[28].

To examine the location of OFUS focus, we visualized the propagation of ultrasound focus by an optoacoustic tomography system. The laser pulse was delivered from the bottom of the SOAP. Both the ultrasound image and optoacoustic (OA) image were detected with a 128-element ultrasound transducer array from the top (Supplementary **Fig. S7**). **Fig. S7** shows merged ultrasound images of SOAP and the mouse skull (Green) and OA image of OFUS (Red) without and with the skull. The ultrasound image was

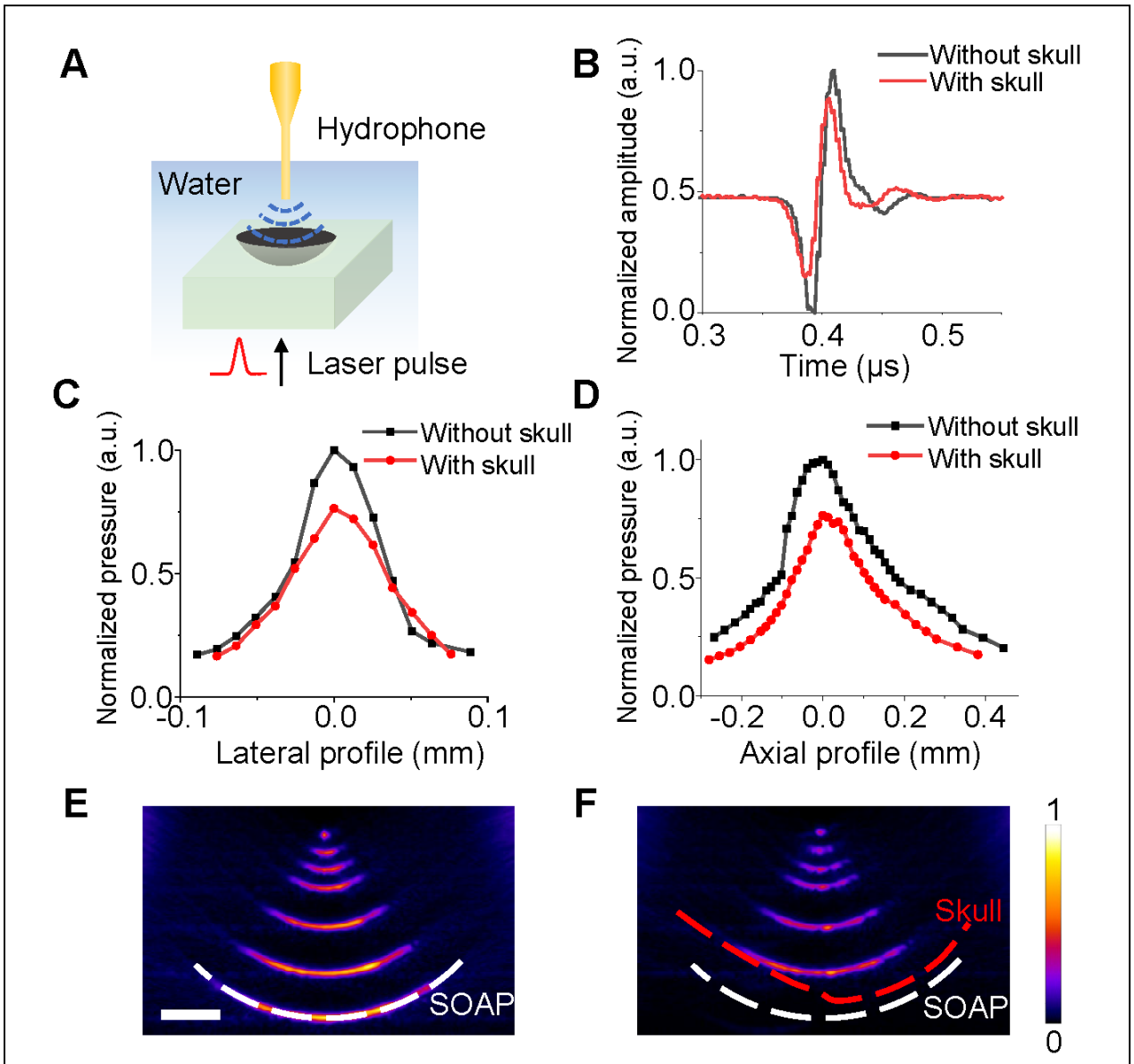

Fig. 2. Transcranial efficiency and high spatial resolution of OFUS penetrating a mouse skull. (**A**) Illustration of experimental setup for charactering OFUS with a needle hydrophone. (**B**) Time domain optoacoustic signals measured at the focus of without and with a mouse skull. Results were normalized to the peak pressure without the skull. (**C**) Lateral resolution of OFUS without and with a mouse skull. (**D**) Axial resolution of OFUS without and with a mouse skull. (**E, F**) OFUS-generated ultrasound propagation without (**E**) and with the skull (**F**). Image scaled to propagation without skull. White dashed line: SOAP. Red dashed line: mouse skull. Scale bar: 2 mm.

measured using the US mode, sending acoustic pulses and receiving echoes back. The OA image was taken using the receiving-only mode for OA signals acquisition. The dashed lines in **Fig. S7** highlighted the surface plane of SOAP and the mouse skull. No significant change in the position of OFUS focus is observed. In **Fig. 2E** and **2F**, by tuning the delay for the ultrasound transducer array, we reconstructed the propagation process of the OFUS from the SOAP surface to the focus area. The delays between OA images are not evenly distributed. These propagation results not

only illustrate the interference of optoacoustic signal to generate a tight focus, but also demonstrate that this interference would not be influenced significantly by the presence of mouse skull, therefore enabling a tight transcranial focus.

2.3 SOAP ENABLES DIRECT AND TRANSCRANIAL STIMULATION OF PRIMARY CORTICAL NEURONS

Along the goal of OFUS stimulation of neural systems, we first investigated whether OFUS can evoke responses in cultured neurons. Primary cortical neurons extracted from rats were transfected to express GCaMP6f. The calcium signal was recorded by a fluorescence imaging system consisted of an inverted wide-field microscope and a CMOS camera. Before the experiment, the light path of the excitation laser for SOAP was aligned with the imaging system. Then, SOAP was mounted by a customized holder to an XYZ translation stage, and carefully adjusted to align with the light path of the excitation laser. SOAP was placed ~ 2 mm above the cultured neuron (**Fig. 3A**). To locate the focus in XY direction, we used 9.9 μm fluorescent beads as indicators. When the laser was on, the position of the ultrasound focus could be visualized by the movement of beads due to acoustic radiation force. Based on the movement of beads, we have identified the diameter of the focus around ~ 100 μm, which is consistent with our tested lateral resolution (**Fig. 2C**).

For neural stimulation, we delivered a single laser pulse at 1064 nm with an 8 ns pulse width, which generated a single optoacoustic pulse. We increased the laser pulse energy from 2.8 mJ/cm^2, with a non-linear step determined by laser filters, until a successful activation defined as max $\Delta F/F >$ 10% was achieved. **Fig. 3B** shows representative calcium images before and after the OFUS stimulation with an input laser energy of 3.5 mJ/cm^2. Neuron activations are only observed at the center of the field of view corresponding to the focus location, showing a localized stimulation ability of OFUS with submillimeter spatial resolution (**Fig. 3B**). A light leakage is observed at the delivery of laser. To assure the activation is not evoked by this leakage, we tuned the laser energy to 2% and delivered it to the neurons directly. No activation of neurons is observed in this control experiment. We calculated the success rate of OFUS stimulation by counting the stimulated neurons to all the neurons within the focus area in each trial. This focus area is defined as a circle with a diameter of 66 μm. Within 6 trials at energy level of 3.5 mJ/cm^2, 10 out of 14 neurons were stimulated. Thus, for CS-PDMS OFUS at a laser pulse energy of 3.5 mJ/cm^2, a success rate of 71.4% was achieved.

Calcium traces from 37 neurons that were successfully activated at the OFUS focus were analyzed (N = 7 dishes). Two types of response are observed, a transient response and a prolonged response. We fitted the decay of the response curves exponentially and obtained the *1/e* time constant. The transient activations typically show decay time constants ranging from 2 to 5 s, while the prolonged activations have time constants of 5 s and up [47]. The transient responses show an average decay time constant of 4.2 s and a max $\Delta F/F$ of 31% ± 8% (N = 6 from 3 cultures, data in mean ± SD) (**Fig. 3C**). The prolonged responses have an average time constant of 7.8 s and max $\Delta F/F$ of 62% ± 12% observed (N = 31 from 4 cultures) (**Fig. 3D**). The prolonged activations are observed at the focus right after a single cycle of OFUS is delivered. This action potential then propagates through the network (Supplementary **Fig. S8**).

We also examined the threshold to evoke transient and prolonged activations and plotted them in **Figure. 3E**. The threshold for the transient responses is found to be 3.8 ± 0.5 mJ/cm^2, significantly lower than that of the prolonged responses, which is 5.7 ± 1.8 mJ/cm^2 (two-sample t-test, N = 37 from 7 cultures, ***p<0.001). Such an ability of neurons differentiates the magnitude of mechanical stimuli and response to higher amplitude

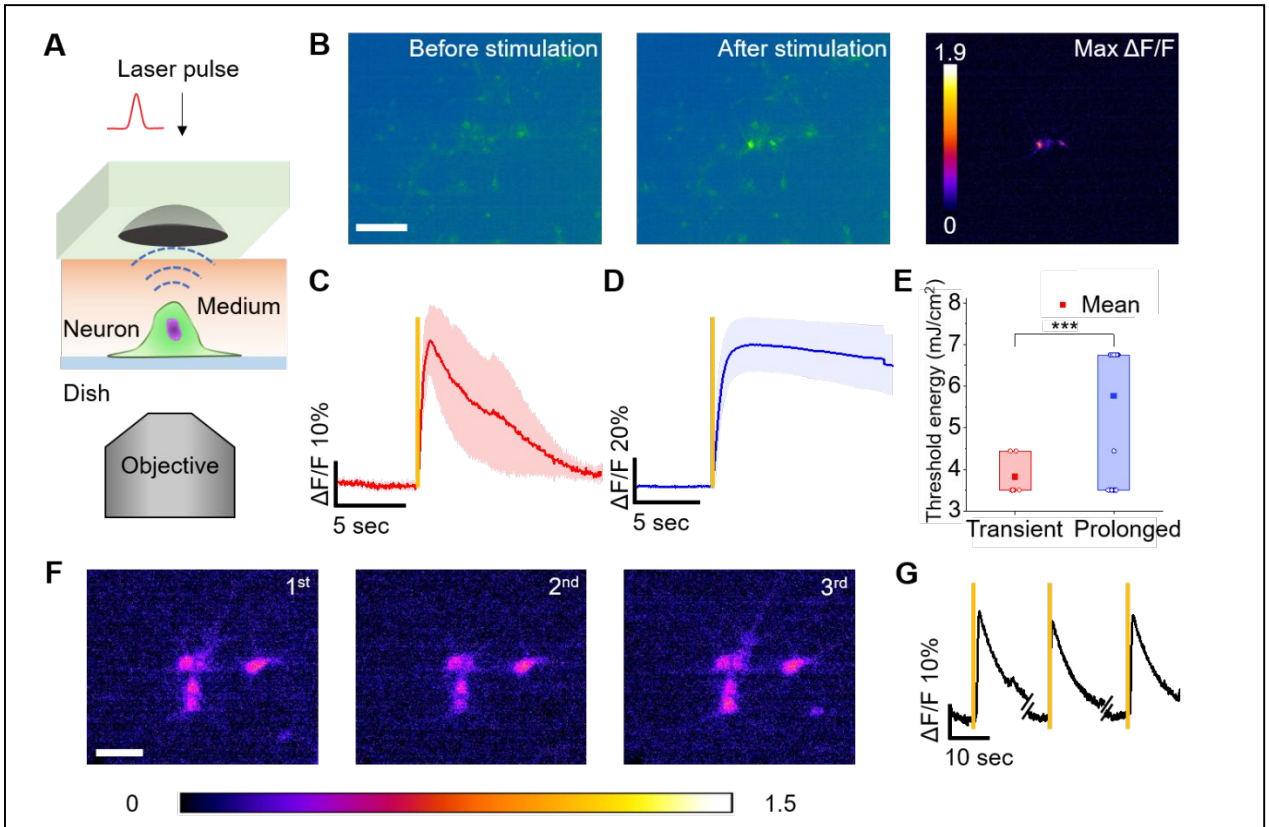

Fig. 3. Cultured neurons are stimulated by OFUS delivered by SOAP *in vitro*. (**A**) Schematic of OFUS stimulation setup. (**B**) Representative calcium images of neurons before and after OFUS stimulation. The right panel shows the maximum ΔF/F. Scale bar: 50 µm. (**C**) Average calcium traces of a transient stimulation. (**D**) Average calcium trace of the prolonged OFUS stimulation. Average traces in solid and SEM in shades. Yellow vertical lines: laser on. (**E**) Statistics of the threshold energy of the transient and prolonged stimulation. ***p < 0.01. (**F**) Maximum ΔF/F image of repeated stimulation for safety demonstration. Scale bar: 50 µm. (**G**) Calcium traces corresponding to the repeated stimulation in E taken from the same neuron. Yellow vertical lines: laser on.

stimulation with a slower decay agrees well with several reports studying neurons response to mechanical stimuli [47, 48].

To demonstrate the safety of OFUS neural stimulation, we firstly studied whether neurons can be stimulated repeatedly. We delivered single-cycle stimulations at the same group of neurons 3 times with an interval of 2 min. The laser energy was kept at 3.5 mJ/cm^2. **Fig. 3F** shows max *ΔF/F* images of each stimulation taken from the calcium imaging, and no visible damage in morphology is observed. The calcium trace (**Fig. 3G**) shows a similar amplitude of max *ΔF/F* after each stimulation, which confirms no functional damage after repeated stimulation. We further tested the viability of neurons using GCaMP6f labelling and propidium iodide (PI) staining after repeated stimulation at 6.5 mJ/cm^2 and 8.4 mJ/cm^2, respectively. These two energy levels were selected 70 % higher than the threshold to leave an extra margin for the safety demonstration. We studied five groups of neurons at each energy level. For each group, we delivered 10 pulses with an interval of 5 s. In each pulse, 3 cycles at 10 Hz were included. To calculate cell viability, we counted live and dead cells within an area of 200 × 200 µm^2 centered at the focus after 30 min incubation. The live cells were counted as those labelled with GCaMP6f

Device	Frequency (MHz)	I_{SPPA} (W/cm^2)	Duration (s)	Total energy density (J/cm^2)
SOAP (this work)	15	2.35×10^5	0.09×10^{-6}	0.02
Transducer (this work)	0.5	3.02×10^4	0.5	1.5×10^4
Transducer [1]	0.3	15	0.5	7.5

Table 1. Experimental conditions and total energy density to evoke similar amplitude of neuron response. Total energy equals to ultrasound intensity times duration.

but not stained with PI. The dead cells were labelled with both signals. A group without laser excitation was performed as a control. No significant difference is observed in the cell viability between the stimulated groups and the control group for both energies (Supplementary **Fig. S9**). These data collectively show that OFUS can stimulate neurons repeatedly and reliably, without any damage to the morphology or functionality of neurons.

To compare OFUS to transducer-based FUS, we performed neural stimulation with a 0.5 MHz conventional focused ultrasound transducer in exactly the same experimental setup as the SOAP experiment *in vitro*. We started with a low ultrasound intensity and a short duration of continuous wave (CW) ultrasound. Then we increased its intensity and duration step by step until a neural response with max $\Delta F/F > 10\%$ was recorded. An ultrasound intensity of 3.02×10^4 W/cm^2 with a 500 ms duration evoked a calcium response up to 18% in our experimental setup (Supplementary **Fig. S10**). Compared to the conventional transducer, OFUS evokes neuron response at a similar level, but with six orders of magnitude less energy. In addition, compared to published work with a conventional transducer to evoke ~ 15% calcium response [1], OFUS stimulation used two orders of magnitude less energy (**Table 1**). Notably, this earlier work used cortical neurons extracted from mouse brains and cultured on a film dish, while our work used cortical neurons from rat brains and cultured on a glass-bottom dish. Together, these results demonstrate the high stimulation efficiency of SOAP with a unique single-cycle stimulation mode that benefits from the optoacoustic effect.

To test the transcranial stimulation capability, we studied the stimulation threshold of cultured neurons with OFUS penetrating a piece of mouse skull. We embedded a piece of mouse skull in the SOAP and then illuminated the SOAP from the top. Fluorescence images of GCaMP6f neuron was recorded from the bottom of the cell culture dish (**Fig. 4A**). The ultrasound focus was aligned by the translation stage and fluorescent beads as previously described. **Fig. 4B** shows the representative images of calcium signal before and after transcranial stimulation by OFUS, and the corresponding max $\Delta F/F$ image. Only the neuron in the middle of the field of view was activated, confirming that the transcranial focus is still tight for high-precision stimulation. With a single cycle stimulation by OFUS, successful stimulations with an average max $\Delta F/F$ of 27% ± 5% were recorded (N = 18 from 7 cultures, **Fig. 4C**). The thresholds for direct stimulation and transcranial stimulation were compared in **Fig. 4D**. While the average threshold for direct stimulations is 5.4 ± 1.5 mJ/cm^2, the transcranial

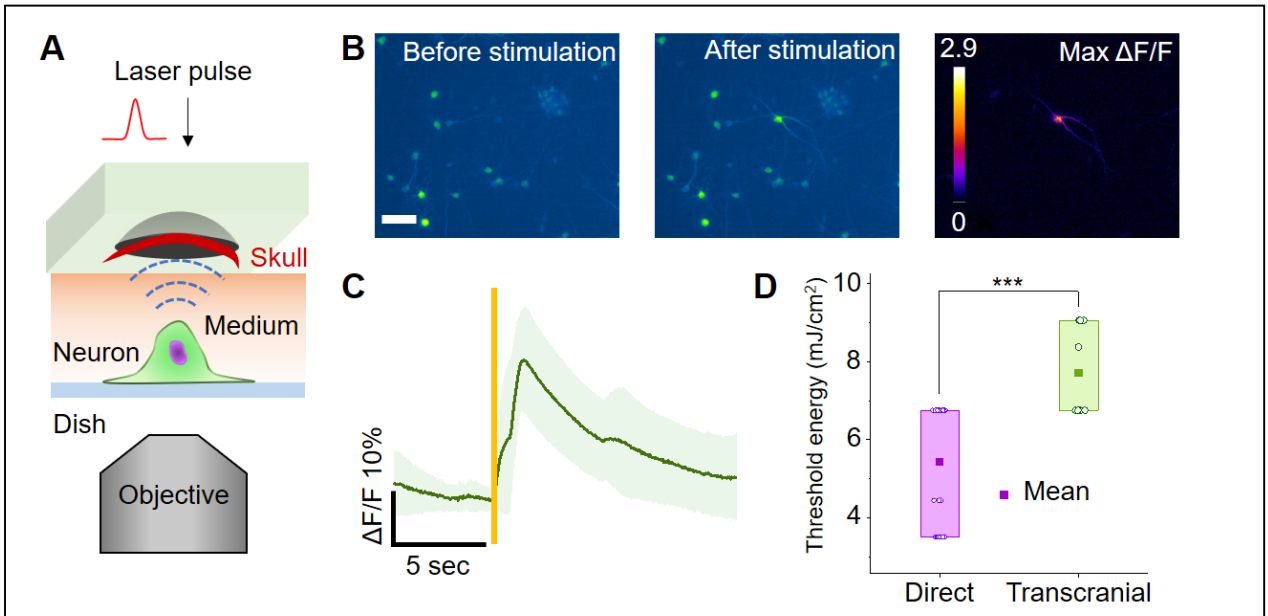

Fig. 4. Transcranial stimulation by OFUS *in vitro*. (**A**) Schematic of transcranial *in vitro* stimulation. (**B**) Representative image of neurons before and after transcranial stimulation. The rightest panel showed the maximum ΔF/F. Scale bar: 50 μm. (**C**) Averaged calcium response trace of transcranial OFUS stimulation. Yellow vertical line: laser on. Average traces in solid and SEM in shades. (**D**) Statistics of threshold energy of direct and transcranial stimulation with single cycle. ***$p < 0.01$.

stimulation has a threshold of 7.7 ± 1.1 mJ/cm^2 (two-sample *t*-test, N = 46 from 11 cultures, ***$p<0.001$). This increase of the laser energy in transcranial stimulation comes naturally due to the energy loss in the transcranial process. Assuming the neurostimulation threshold remains during different trials, the input energy of 5.4 mJ/cm^2 need to reach 7.7 mJ/cm^2 to compensate for the previously tested transcranial efficiency of 69%. This theoretical value is consistent with our experimental transcranial stimulation threshold. Collectively, our results demonstrate the ability of OFUS to stimulate cortical neurons both directly and transcranially.

2.4 OFUS MEDIATES HIGH-PRECISION NEURAL STIMULATION IN VIVO

With successful stimulations of cultured neurons directly and transcranially, we further asked whether OFUS can activate neurons in a living animal brain. Adult C57BL/6J mice were used for stimulation *in vivo*, and the effect of stimulation was evaluated by both immunofluorescence imaging and electrophysiology recording. Mice were deeply anesthetized with isoflurane and shaved to expose the scalp. We mounted a CS-PDMS SOAP to a customized 3D-printed holder and attached it to an XYZ translation stage. The input laser was delivered from the top, and the focus of generated ultrasound was carefully aligned with the motor cortex based on stereotaxic coordinates (Medial-Lateral: 1.5, Anterior-Posterior: 0.5) [49] (**Fig. 5A** and supplementary **Fig. S11**).

We firstly visualized the stimulated area by labeling c-Fos proteins in stimulated neurons. The expression of c-Fos protein has been widely used to identify stimulated neurons [50]. To induce robust c-Fos expression, we applied OFUS stimulation with laser energy of 1.0 mJ/cm^2 (corresponding to a peak-to-peak pressure of 39 MPa) for a pulse train of 20 pulses

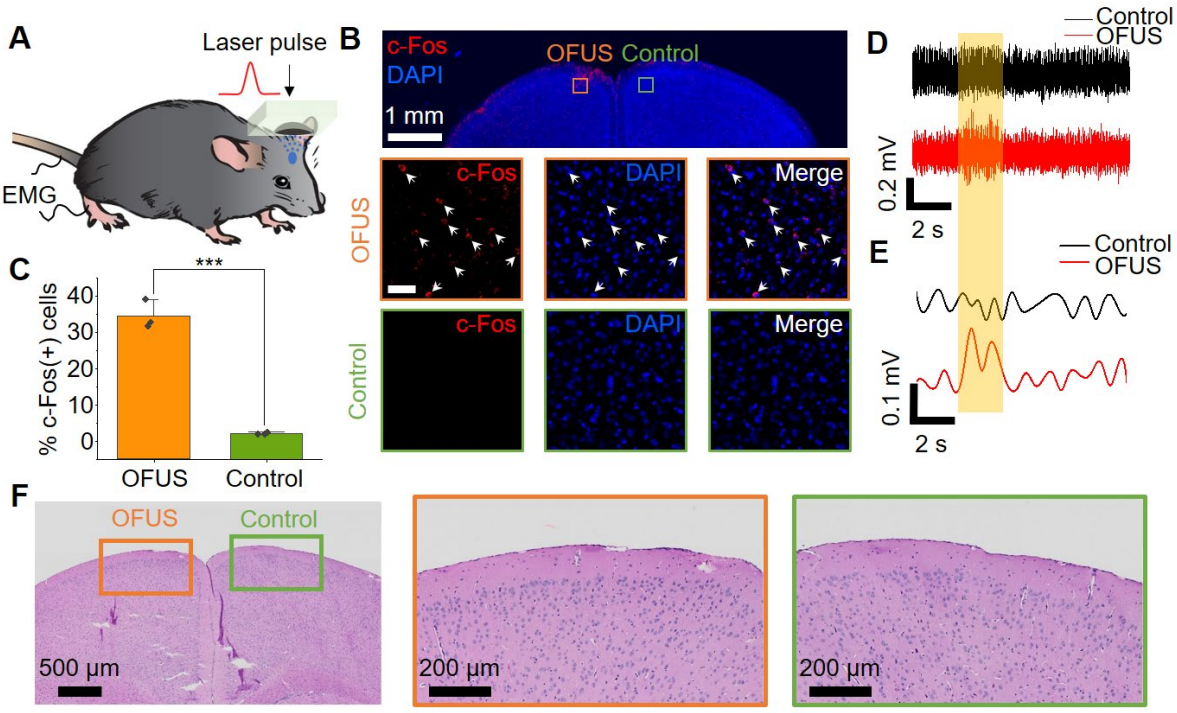

Fig. 5. Representative immunofluorescence examinations and EMG recording traces for *in vivo* OFUS stimulation. (**A**) Schematic of OFUS stimulation *in vivo*. (**B**) Representative image of c-Fos and DAPI staining within the stimulation and control area. Red: c-Fos. Blue: DAPI. Orange outline: OFUS stimulated area. Green outline: control group at contralateral area. Scale bar: middle and lower panel, 50 µm. (**C**) Statistic analysis of percentage of c-Fos positive neurons. ***p<0.001, two-sample *t*-test. (**D**) Representative EMG recording of 2 s OFUS stimulation and no light control group. Orange box: laser on. (**E**) EMG signal after band-pass filter and full-wave rectifier and envelope. (**F**) Histology results after stimulation *in vivo*.

at 10 Hz, which lasted 30 min with a 33% duty cycle (Supplementary **Fig. S12**). The mice were put to rest for 1 h to maximize c-Fos expression [51]. The mouse brain was then extracted and fixed in 10% formalin for 24 h. Brain slices of 150 µm thickness were stained with c-Fos and DAPI and imaged under a confocal microscope. DAPI can label all the nucleus of neurons and provide a reference. Thus, the c-Fos positive neurons were counted only when it co-localized with DAPI signal. The c-Fos positive cells observed at the OFUS-stimulated area are much more than the control group at the contralateral area (**Fig. 5B**). We calculated the ratio of c-Fos positive cells and the DAPI stained cells in the OFUS group and the control group. The percentage of c-Fos positive in the OFUS group is 34 ± 4 %, a significant increase from 2 ± 0.3 % in the control (**Fig. 5C**, two-sample *t*-test, n = 3, ***p<0.001). Importantly, the c-Fos signal is confined to the target site with an area of ~ 200 µm in diameter, close to the focus size of OFUS. This result demonstrates superior spatial resolution compared to conventional PZT-transducer-based tFUS stimulation (1 ~ 5 mm) [28]. No significant c-Fos expression outside the targeted area was observed, confirming direct OFUS stimulations. These results collectively suggest the ability of OFUS to directly evoke responses of neurons non-invasively with a high spatial resolution of 200 µm.

Further evaluation of the functional outcome by OFUS stimulation was conducted with the electromyography (EMG) method. The focus of OFUS was aligned to the primary motor cortex of

the mouse brain to evoke cramps of muscles. To record muscle activities, the EMG electrode was inserted parallel to the biceps femoris muscle into the hind limb, and the ground electrode was inserted into the tail (**Fig. 5A**). A laser pulse train with a duration of 2 s at 1.0 mJ/cm^2 was delivered to SOAP. Strong EMG responses (0.458 ± 0.03 mV) were recorded from the contralateral hind limb (**Fig. 5D**). Those EMG signals have a typical delay of ~ 61 ± 6 ms between laser onset and EMG response. After processed with a bandpass filter and full-wave rectifier, the envelopes of the EMG signals are plotted (**Fig. 5E**). To eliminate the possibility of EMG response evoked by the auditory effect of ultrasound, we stimulated at the somatosensory cortex based on stereotaxic coordinates as a control. No significant EMG response is observed in the control group. This result suggests that the EMG response was evoked directly by OFUS stimulation without the involvement of the auditory pathway.

Next, we evaluated the safety of OFUS stimulation *in vivo* by hematoxylin and eosin (H&E) staining. After the EMG recording, mice were sacrificed, and brains were extracted and fixed. Brain slices of 5 μm thick were obtained every 150 μm and standard H&E staining was performed. We examined all the brain slices by a slice scanner and compared between targeted area and the control group at the contralateral area. No significant change in morphology of cells between those groups is observed (**Fig. 5F**). This result illustrates that the OFUS stimulation does not induce visible damage to mouse brains.

The biosafety of OFUS is crucial for successful neuromodulation. In this work, biosafety was evaluated by cell viability after repeated stimulation *in vitro* and histological imaging *in vivo* where no damage was concluded. Additionally, cavitation and thermal accumulation are two major potential bioeffects of ultrasound exposure. To evaluate the potential impact of these effects under the operation condition of OFUS, we calculated the mechanical index (MI) and tested the temperature rise of OFUS. With our laser input used in *in vivo* experiment, the estimated peak-to-peak pressure 39 MPa delivered to the mouse brain is below the level of 40 MPa in which no tissue lesion was reported previously [52]. The peak negative pressure of OFUS was measured to be 18 MPa, which is below the threshold of bubble cloud generation in soft tissue (25-30 MPa) [53, 54]. An MI of 3.3 is obtained for OFUS stimulation based on acoustic attenuation coefficient for brain tissue of $0.91\,\mathrm{dB/(cm \times MHz)}$ [55]. In comparison, short-pulse ultrasound exposure with a pulse duration of 1.4 μs at MI = 3.9 has been reported with rare cavitation-related damage in brain tissue [56]. Thus, our shorter pulse duration of 0.09 μs and lower MI are believed to be well below the damage threshold for tissue cavitation.

For thermal safety, the temperature profiles were recorded with a thermocouple. We applied the laser energy of 6.2 mJ/cm^2, which matched the highest energy threshold used in this work. We delivered OFUS for 10 s. A temperature elevation up to 0.4 K is observed at the surface of SOAP (Supplementary **Fig. S13**). No temperature increase is observed at the other two groups: tested at the focus of OFUS with laser on and baseline tested at the surface of SOAP without laser. Therefore, even with longest duration of 2 s used in the successful stimulation, temperature rise induced by OFUS is expected to be less than 0.1 K at the focus of OFUS. Furthermore, the temperature rise is still far below the threshold required to thermally modulate neuron activities ($\Delta T \geq 5$ K) [57]. Therefore, OFUS has been demonstrated to be safe for brain modulation both biologically and physically.

3 DISCUSSION

In this work, we developed a CS-PDMS SOAP for OFUS generation, characterized its spatial resolution and transcranial ability, and validated the submillimeter transcranial neural stimulation *in vitro* and *in vivo*. The large NA from the SOAP allows a tight lateral focus of 66 μm, which is beyond the reach of the piezo-based low-frequency ultrasound. OFUS provides a transcranial efficiency of 69 %, which enables the transcranial applications. Direct and transcranial stimulations of GCaMP6f labeled rat cortical

neurons *in vitro* were recorded. A success rate of 71% was achieved with laser energy of 3.5 mJ/cm^2. The total ultrasound energy input of OFUS to evoke neural response is two to six orders of magnitudes lower than conventional ultrasound. Successful non-invasive OFUS stimulation at the motor cortex of living mice *in vivo* was demonstrated by immunofluorescence imaging and EMG recording. The spatial resolution *in vivo* was found to be 200 μm. The safety of OFUS stimulation was confirmed both *in vitro* and *in vivo* by cell viability and histology analysis, and by MI and temperature rise measurements.

An important observation about OFUS stimulation is that the stimulation was evoked by the direct effect of the acoustic wave instead of auditory confounding effect [58, 59]. In experiments *in vitro*, cultured neurons responded to the OFUS stimulation without auditory circuits. In studies *in vivo*, c-Fos positive neurons were located at the stimulation site corresponding to the direct stimulation. Moreover, no EMG response was recorded in the control group which was stimulated at the somatosensory cortex, indicating that the bone conduction to the cochlear is not involved in the process. Such observation agrees with reported direct stimulation with ultrasound[1, 31].

The mechanism of evoking a neural response with ultrasound is still under investigation. While focused ultrasound can induce several physical effects on biological tissue through direct stimulation, such as thermal accumulation, cavitation, and mechanical force, it has been debated whether these bioeffects could lead to neural stimulation [1, 57, 60-63]. The thermal effect has been reported as a plausible mechanism of ultrasound neuromodulation [64, 65]. It has been evaluated by simulation that with frequency from 0.3 to 5 MHz, sonication duration from 80 ms to 20 min, duty cycle from 5 to 100%, temperature rise in the rodent brain is below 1 K [64]. We define the duty cycle of a single-cycle stimulation to be the cycle duration in one second. A single-cycle of OFUS has evoked responses in cultured neurons with a duty cycle of $9 \times 10^{-6}\%$. OFUS has successfully stimulated neurons *in vivo* at 10 Hz, with a duty cycle of $9 \times 10^{-5}\%$. These extra low duty cycles minimized heat accumulation for longer pulse trains. The maximum temperature rise in OFUS was also experimentally evaluated to be < 0.1 K. Therefore, the thermal stimulation mechanism for OFUS can be ruled out. The intramembrane cavitation is a prevailing explanation of how ultrasound perturbs neurons. A model was set up to study how mechanical energy of CW ultrasound is absorbed by the cellular membrane and induces intramembrane cavitation [61]. It requires 2 to 12 cycles for cavitation to reach a stable level and further oscillating with US. The cavitation would further change the capacitance and induce a capacitive current. This current would then activate voltage-gated channels and produce an action potential [63]. The cavitation mechanism induced by the CW mode doesn't apply to OFUS, because the single cycle stimulation of OFUS would be too short for forming a stable gas bubble and keep it oscillating to perturb the ion channels. Therefore, we ruled out the cavitation mechanism for OFUS stimulation. The radiation force is another plausible explanation believed dominants high-frequency ultrasound stimulation [41, 66, 67]. Successful stimulation of neurons has been demonstrated with the radiation force by activating mechanosensitive channels with [41] or without [1] mechanical displacement at micron-scale. Radiation force was also reported to induce the change of capacitance in the lipid bilayers at the "On" and "Off" of ultrasound [68]. The effect of the radiation force of OFUS has already been visualized by the movement of beads in our work. Further work to study whether the radiation force delivered by OFUS can activate mechanosensitive channels or voltage-gated channels will elucidate the mechanism of OFUS stimulation. One difference between previous studies in radiation force and OFUS is that previous studies focused on CW ultrasound while OFUS is a unique transient radiation force at a sub-μs level. This time scale is unlikely to directly trigger ion channels, which is normally at ~ 100 ms scale. OFUS possibly changes the capacitance of the membrane drastically with a greater ultrasound intensity, which is consistent with reported findings [41]. Further investigation

is needed to identify whether there is a unique OFUS mechanism.

Brains are complex and many functions are not controlled by a single site. Multisite stimulation provides more possibilities in modulation and therapies. Patterned neuromodulation, for example, can further provide selectivity in motor control for therapy [69, 70]. For conventional PZT-based ultrasound massive array, the massive cablings connected to each element are fabricated with copper to minimize electromagnetic interference, which further impedes the application of a wearable clinical device. Taking advantage of optical engineering, the OFUS device can be scaled up into a massive array for multisite neuromodulation. A light-weighted OFUS device also provides improved accessibility and wearability for long-term treatments. In addition, OFUS devices, with no metal components, further offer improved compatibility with real-time magnetic resonance imaging (MRI) guidance and functional MRI monitoring. These features of OFUS enable real-time fMRI evaluation of stimulation treatment and open up opportunities for close-loop treatments in clinical applications.

Notably, OFUS can provide high ultrasound intensity by simply improving the energy of input light [43], offering an opportunity for treatment in lieu of conventional high intensity focused ultrasound (HIFU). For example, histotripsy delivers low frequency (< 3 MHz), short pulses (< 10 cycles) of high intensity ultrasound (> 20 MPa) into tissue for cavitation-based therapy [71, 72]. However, HIFU needs high voltage to reach a certain intensity, which meanwhile leads to a narrow bandwidth (< 30%), a long ringdown time (> 5 cycles), and a risk of dielectric breakdown [72]. Our OFUS generated by SOAP has demonstrated high frequency, high intensity, precise single-cycle control, and a broad bandwidth of 200%. This niche highlights a future direction of OFUS application in ultrasound surgery with improved spatiotemporal control, minimized damage, and heat accumulation to surrounding tissues.

Current parameters of tFUS neurostimulation, employing either continuous wave or pulsed scheme with consecutive cycles, leads to the formation of the standing wave [73, 74]. The mismatch of acoustic impedance at interfaces of skull-tissue and tissue-air makes the skull a cavity reflecting acoustic waves and resonating with consecutive cycles. The local maxima in standing waves have adverse effect on precise targeting by affecting off-target area, and can further cause heat accumulation or cavitation and damage tissues [75, 76]. Therefore, extra efforts are needed in designing a transducer-mounted diffusers to deliver incoherent ultrasound [73]. OFUS, on the contrary, can inherently eliminate the formation of the standing wave. Firstly, optoacoustic signal has a broader bandwidth than a PZT-based transducer. According to the following equation of the coherent length, a shorter coherent length L can be provided by OFUS:

$$L = \frac{v}{\Delta f} \tag{3}$$

In this equation, v and Δf stand for ambient sound speed and bandwidth of the generated ultrasound, respectively. With a bandwidth of 200%, the coherent length of OFUS is 4 times shorter than a PZT-based transducer with a typical bandwidth of 50% [77, 78]. A shorter coherent length leads to a weaker acoustic interference. Secondly, OFUS has the acoustic frequency in MHz range that induced by nanosecond laser pulses at several kHz or lower, which maintains the broad bandwidth of photoacoustic signals. With a proper selection of the repetition rate of the laser, for example, 2 kHz in sub-MHz range, OFUS can be delivered with an ultra-low duty cycle. In frequency domain, the off between laser frequency and acoustic frequency maintains the broad bandwidth of photoacoustic signal. This key feature of OFUS brings a very weak interference ability of the whole OFUS pulse train, making the formation of standing waves in skull cavities improbable.

In summary, OFUS offers submillimeter precision non-invasively towards neurological research in sub-regions of a brain. Its flexibility in fabrication, high spatiotemporal resolution,

and improved electromagnetic compatibility further allow clinical applications, such as ultrasound surgery, drug delivery, and pain management. This work thus underlines the potential for OFUS to be utilized as a valuable platform technology in neuroscience research and clinical therapies.

MATERIALS AND METHODS

Simulation of the ultrasound field

The ultrasound field generated by SOAP was simulated in 2D by an open-source k-Wave toolbox on MATLAB R2019b (MathWorks, MA). No light absorption was considered during the simulation. SOAP was delivering ultrasound into the water as the propagation medium. The backing material was set to air. The density and acoustic speed of different materials were defined accordingly.

Fabrication of HSM-SOAP

To form a curvature, a ~20 mm piece of heat-shrink tubing (McMaster-Carr, 6363K214) was filled with a steel bead with a diameter of 12.7 mm (McMaster-Carr, 9529K22), and heated up with a heat gun to fully shrink. After that, we cut the tubing 2 mm away from a great circle of the steel bead and obtained an HSM-SOAP.

Fabrication of CNT-PDMS and CNP-PDMS SOAPs

5 wt% multi-wall carbon nanotubes (VWR, MFCD06202029) and CNP (Sigma-Aldrich, 633100-25G) were mixed with the PDMS base and curing agent matrix (10:1 weight ratio, Dow Corning Corporation, Sylgard 184), respectively. The mixture was poured into a 3D-printed mold designed with a 12.7 mm diameter and 2 mm focal distance and degassed in vacuum for 30 min. To get fully cured CNT-PDMS and CNP-PDMS SOAPs, the mixture was heated in an oven to 60 °C for 2.5 hrs before being removed from the mold.

Fabrication of CS-PDMS SOAP

A steel bead with a diameter of 12.7 mm was placed at the flame core of a paraffin wax candle for 10 to 15 s to be fully coated with flame synthesized candle soot nanoparticles. Then, the coated bead was dipped into the degassed PDMS base and curing agent matrix (10:1 weight ratio) and positioned so that the surface of the PDMS matrix is 2 mm lower than the great circle plane of the bead. The cured sample was obtained after 15 min heating at 110 °C on a heat plate.

OFUS generation and characterization

A Q-switched Nd: YAG laser (Quantel Laser, CFR ICE450) delivered 8 ns pulses at 1064 nm to SOAP to generate an optoacoustic signal from the SOAP. The laser was modulated by a function generator (33220A, Agilent) at a repetition rate of 10 Hz. A system consisting of a 40 μm needle hydrophone (Precision Acoustic, MH0040, optimized for 5 to 40 MHz range), a submersible preamplifier, and a DC coupler was used for the ultrasound pressure and waveform measurement. The waveform was amplified with an ultrasonic pulser-receiver (Olympus, Model 5073PR) and collected with a digital oscilloscope after 4 times average (Rigol, DS4024). As the needle hydrophone has a tip of 40 μm smaller than the generated focus, the acquired data P_{peak} only reflects the pressure in the sub-regions of the focus area. To get an estimation of the real pressure over the entire ultrasound focus, a 25.4 μm step was taken to map out the pressure over the focus area. The data was averaged to get spatially averaged pressure $P_{averaged}$. A coefficient C was obtained by the following equation $C = P_{averaged}/P_{peak}$. The hydrophone has an upper limit at 50 MPa of linear range. Exceeding this pressure may cause damage to the device. When the reading reached close to 50 MPa, we recorded current pressure P_0, moved the hydrophone out of focus area and recorded a pressure $P_{0\text{-}out}$. Then, we increased the laser energy and recoded a pressure $P_{x\text{-}out}$. This helped us to estimate the pressure at the focus P_x

generated by current energy input by the following equation $P_x = \frac{P_{x-out}}{P_{0-out}} P_0$, due to constant spatial pressure distribution. The final estimated spatially averaged pressure was acquired by multiplying P_x with coefficient C.

SEM imaging of SOAP

Before SEM imaging (Zeiss, Supra 55VP), thin cross-section slices of SOAP were sputtered with Au/Pd for 10 s and mounted on an aluminum stub. SEM images of SOAP were obtained at 3kV as accelerating voltage with an aperture size of 20 microns.

SRS and photothermal imaging of SOAP

An 80-MHz femtosecond pulsed laser (Spectra-Physics, InSight X3) provides a tunable beam (from 680 nm to 1300 nm) and a synchronized beam (fixed at 1045 nm) for the multimodal imaging system. To image the PDMS and candle soot, the tunable beam was set to 801 nm as the pump beam, along with the fixed wavelength beam as the Stokes for femtosecond stimulated Raman scattering (SRS) imaging of C-H bonds and also the probe beam for pump-probe imaging of candle soot simultaneously. After the Stokes/probe beam was modulated by an acoustic-optic modulator (Isomet Corporation, 1205c), the pump and Stokes/probe beams were combined by a dichroic mirror and directed into a lab-built laser scanning microscope. The temporal delay between the pump and Stokes/probe pulses was controlled by a motorized delay stage. A 60× water objective (Olympus, UPlanApo 60XW, NA=1.2) focused the collinear beams onto the sample. The power of each beam on the sample was 2 mW. The two beams were collected in the forward direction by an oil condenser (Olympus, Aplanat Achromat 1.4, NA=1.4) and then filtered by short pass filters. After filtering, only the pump beam was detected by a photodiode with a laboratory-built resonant amplifier. A lock-in amplifier (Zurich Instrument, MFLI) demodulated the detected pump beam for the stimulated Raman loss signal and the pump-probe signal according to the modulation transfer. The femtosecond SRS of C-H bonds in PDMS only occurs when the two beams temporally overlapped (t ~ 0 s) while the candle soot's pump probe photothermal signal has a much longer decay. Thus, an x-y-t image stack was acquired to decompose the distribution of the CS-PDMS mixture. A chemical composition map can be generated by applying least square fitting with the time domain references from the pure samples. This strategy allowed simultaneous SRS imaging of PDMS and photothermal imaging of candle soot.

Optoacoustic tomography imaging

An optoacoustic tomography system consists of a customized 128-element transducer array (L22-14v, Verasonics Inc., 50 % bandwidth) and a 128-channel ultrasound data acquisition system (Vantage 128, Verasonics Inc.). The PAT system is synchronized to the Quantel laser by a function generator and a delay generator (DG535, Stanford Research Systems). The function generator triggered the Quantel laser and the delay generator with a pulse mode at a 10 Hz repetition rate. The delay generator added another tunable delay to the Vantage 128 to receive ultrasound signals at different time delays after the optoacoustic signal was generated. By tuning the delay, propagation of the optoacoustic signal can be visualized.

Embryonic neuron culture

All experimental procedures have complied with all relevant guidelines and ethical regulations for animal resting and research established and approved by the Institutional animal care and use committee of Boston University (PROTO201800534). 35 mm glass-bottomed dishes were coated with 50 μg/ml poly-D-lysine (Sigma-Aldrich), placed in an incubator at 37 °C with 5% CO_2 overnight, and washed with sterile H_2O three times before seeding the neuron. Primary cortical neurons were derived from

Sprague-Dawley rats on embryonic day 18 (E18) of either sex and digested in papain (Thermo Fisher.). A medium with 10% heat-inactivated fetal bovine serum (FBS, Atlanta Biologicals), 5% heat-inactivated horse serum (HS, Atlanta Biological), 2 mM Glutamine Dulbecco's Modified Eagle Medium (DMEM, Thermo Fisher Scientific Inc.) was used for washing and triturating dissociated cells. Cells were cultured in cell culture dishes (100 mm diameter) for 30 min at 37 °C in a humid incubator to eliminate fibroblasts and glial cells. The supernatant containing neurons was collected and seeded in poly-D-lysine coated dishes with 10% FBS + 5% HS + 2 mM glutamine DMEM medium. After 16 h, the medium was replaced with Neurobasal medium (Thermo Fisher) containing 2% B27 (Thermo Fisher), 1% N2(Thermo Fisher), and 2 mM glutamine (Thermo Fisher). 5 μM 5-fluoro-2′-deoxyuridine (Sigma-Aldrich) and AAV9.Syn.Flex.GCaMP6f.WPRE.SV40 virus (Addgene, MA, USA) at 1 μl/ml final concentration was added to the medium at day 5, for preventing glial proliferation and expressing GCaMP6f, respectively. 50% of the medium was replaced with a fresh culture medium every 3 to 4 days, and neurons were used for stimulation after 10 to 13 days.

OFUS stimulation *in vitro*

SOAP was mounted on a 3D-printed holder to a translation stage for fine adjustment of the device position. The Quantel laser was delivered to SOAP in free space for optoacoustic signal generation. An inverted microscope (Eclipse TE2000-U, Nikon) with 10X objective (Plan Fluor, 0.3 NA, 16 mm WD, Thorlabs) was used for fluorescence imaging. The microscope was illuminated by a 470-nm LED (M470L2, Thorlabs), filtered by a filter set for green fluorescent protein (MDF-GFP, Thorlabs), and imaged with a CMOS camera (Zyla 5.5, Andor). Before stimulation, the focus of ultrasound was visualized by the motion of 9.9 μm green fluorescent beads (G1000, Duke Scientific Corp) dispersed in water. The focus was then adjusted to the center of the field of view, so that once the neuron culture dish was placed on the sample stage, the neurons at the center of the view field would be at the OFUS focus. After we switched to neuron culture, SOAP was placed 2 mm above the neuron in the Z direction to ensure the focus can reach neurons. The CMOS camera was synchronized with the laser. The fluorescence intensities in imaging sequences were analyzed with ImageJ (Fiji) after experiments.

Cell viability study

For cell viability studies, we randomly selected five groups of neurons at the OFUS focus in each dish at selected energy level. Each group of neurons was delivered 30 pulses of OFUS in total. Every 3 consecutive cycles were delivered at 10 Hz with an interval of 5 s. All the cells were labelled with GCaMP6f. The dead cells were stained with 1 μL 100 μg/Ml propidium iodide (P1304MP, Thermo Fisher Scientific Inc.) solution for 15 min. The cells were incubated for 30 min before imaged with fluorescence microscope for analysis. The live cells were distinguished with positive GCaMP6f without PI staining. The dead cells were labelled with both GCaMP6f and PI. The live and dead cells within an area of 200 × 200 μm^2 at the focus were counted.

OFUS stimulation *in vivo*

Adult C57BL/6J mice (age 14-16 weeks) were initially anesthetized with 5 % isoflurane in oxygen and then fixed on a standard stereotaxic frame with 1.5 ~ 2 % isoflurane. A tail pinch was used to determine the anesthesia depth. A heating pad was placed under the mouse to maintain the body temperature. The hair on the targeted brain was removed. SOAP mounted on a 3D-printed holder was aligned to the targeted motor cortex of the mouse. The Quantel laser was delivered to SOAP in free space at a 10 Hz repetition rate. For c-fos expression, a pulse train was delivered with 33% duty cycle (2 s laser on, 4 s laser off) for 30

min. For EMG recording, a pulse train of 2 seconds was delivered.

EMG recording and signal processing

The OFUS focus was aligned with the primary motor cortex (ML: 1.5, AP: 0.5). To record the muscle activity, the needle electrode was inserted subcutaneously into the hind limb biceps femoris muscle and the ground electrode was inserted into the tail. The control group was recorded on the trunk ipsilateral to the stimulation site. EMG signals were recorded by a Multi-Clamp 700B amplifier (Molecular Devices), filtered at 1 to 5000 Hz, digitized with an Axon DigiData 1,550 digitizer (Molecular Device), and filtered by a noise eliminator (D-400, Digitimer). EMG signal was filtered with bandpass filter at 0.5 ~ 500 Hz and full-wave rectification. Then the envelope of the processed signal was plotted.

Immunofluorescence staining and imaging

After the stimulation session, the mouse was put to rest for 1 h for maximized c-fos expression, then was sacrificed and perfused transcardially with phosphate-buffered saline (PBS, 1X, PH 7.4, Thermo Fisher Scientific Inc.) solution and 10% formalin. After fixation, the brain was extracted and fixed in 10% formalin solution for 24 hrs. The fixed mouse brain was immersed in 1X PBS solution. The brain was sliced to coronal sections with a 150 μm thickness using an Oscillating Tissue Slicer (OST-4500, Electron Microscopy Sciences). Brain slices were gently transferred by a brush into 10% formalin solution for another 24 h fixation, then blocked with 5% Bovine serum albumin (Sigma-Aldrich)-PBS solution for 30 min at room temperature. The slices were permeabilized with 0.2% Triton (Triton X-100, 1610407, Bio-Rad Laboratories)-PBS solution for 10 min, and incubated with Anti c-Fos Rabbit antibody (4384S, Cell Signaling Technology) at a concentration of 2 μg/mL at 4 °C overnight. Following primary incubation, slices were incubated with secondary antibody Alexa Fluor 488 goat anti-rabbit IgG (Thermo Fisher Scientific) at a concentration of 1 μg/mL and DAPI (Thermo Fisher Scientific) at 5 μg/mL in dark for 2 h at room temperature. Between steps, the slices were rinsed with 0.2% Tween (Tween 20, Tokyo Chemical Industry)-PBS solution 4 times for 5 min. Fluorescent images were acquired with an FV3000 Confocal Laser Scanning Microscope (Olympus). Confocal images were acquired under an excitation wavelength of 405 nm for DAPI and 488 nm for c-Fos.

Histology examination

After the stimulation session, the mouse was sacrificed immediately, and perfused and fixed as previously described. The brain was embedded in paraffin and sliced for 5 μm thickness at 150 μm step to obtain coronal sections. Slicing and standard H&E staining were performed at Mass General Brigham Histopathology Research Core. Histology images were acquired with a VS120 Automated Slide Scanner (Olympus).

Temperature measurement

A thermocouple (DI-245, DataQ) was used to record the temperature profile. The tip of the thermocouple was placed at the focus and the surface of SOAP, respectively. The laser with energy of 6.2 mJ/cm^2 was turned on for 10 s at 10 Hz during recording. Temperature at the SOAP surface without light was also recorded as a baseline.

Statistical analysis

Acoustic waveforms, calcium traces, and electrophysiological traces were plotted with Origin 2020. FFT for the frequency spectrum was performed with MATLAB R2019b. Data are presented with the mean ± standard error of the mean. Calcium images were processed with ImageJ. All comparative data were analyzed with a two-sample *t*-test. p values were defined as: n.s., not significant ($p > 0.05$); * $p < 0.05$; ** $p < 0.01$; *** $p < 0.001$.

ACKNOWLEDGEMENT

Funding: This work is supported by R01 NS109794 to J.-X.C. and C. Y. and R01 HL125385 to J.-X.C

Author contributions: LL and JXC conceived the idea of SOAP; YL simulated, fabricated, and characterized SOAP; YL and YJ designed and performed biology experiments; XG performed SRS and photothermal experiments; YL and RC performed SEM imaging; YL and YZ performed confocal imaging; YL, YJ, LL, XG, YZ, NZ, CY and JXC discussed and analyzed the data; YL and LS prepared neuron cultures; GC and RW helped with data collection; YL wrote the original draft of manuscript; LL, YJ, GC, CY and JXC reviewed and edited the manuscript. CY and JXC supervised the project.

Competing interests: Authors declare that they have no competing interests.

Data and materials availability: All data are available in the main text or the supplementary materials.

REFERENCES

1. Yoo, S., et al., *Focused ultrasound excites cortical neurons via mechanosensitive calcium accumulation and ion channel amplification.* Nature Communications, 2022. **13**(1): p. 493.
2. Mehić, E., et al., *Increased Anatomical Specificity of Neuromodulation via Modulated Focused Ultrasound.* PLOS ONE, 2014. **9**(2): p. e86939.
3. Choi, T., et al., *A Soft Housing Needle Ultrasonic Transducer for Focal Stimulation to Small Animal Brain.* Annals of Biomedical Engineering, 2020. **48**(4): p. 1157-1168.
4. Kim, S., et al., *Transcranial focused ultrasound stimulation with high spatial resolution.* Brain Stimulation, 2021. **14**(2): p. 290-300.
5. Legon, W., et al., *Neuromodulation with single-element transcranial focused ultrasound in human thalamus.* 2018. **39**(5): p. 1995-2006.
6. Rosin, B., et al., *Closed-loop deep brain stimulation is superior in ameliorating parkinsonism.* Neuron, 2011. **72**(2): p. 370-384.
7. Mayberg, H.S., et al., *Deep brain stimulation for treatment-resistant depression.* Neuron, 2005. **45**(5): p. 651-660.
8. Boon, P., et al., *Deep brain stimulation in patients with refractory temporal lobe epilepsy.* Epilepsia, 2007. **48**(8): p. 1551-1560.
9. Ineichen, C., N.R. Shepherd, and O. Sürücü, *Understanding the Effects and Adverse Reactions of Deep Brain Stimulation: Is It Time for a Paradigm Shift Toward a Focus on Heterogenous Biophysical Tissue Properties Instead of Electrode Design Only?* Front Hum Neurosci, 2018. **12**: p. 468.
10. Boyden, E.S., et al., *Millisecond-timescale, genetically targeted optical control of neural activity.* Nat Neurosci, 2005. **8**(9): p. 1263-8.
11. Zhang, F., et al., *Circuit-breakers: optical technologies for probing neural signals and systems.* Nat Rev Neurosci, 2007. **8**(8): p. 577-81.
12. Zhang, F., et al., *Multimodal fast optical interrogation of neural circuitry.* Nature, 2007. **446**(7136): p. 633-9.
13. Chen, R., et al., *Deep brain optogenetics without intracranial surgery.* Nature Biotechnology, 2021. **39**(2): p. 161-164.
14. Gong, X., et al., *An Ultra-Sensitive Step-Function Opsin for Minimally Invasive Optogenetic Stimulation in Mice and Macaques.* Neuron, 2020. **107**(1): p. 38-51.e8.
15. Wagner, T., A. Valero-Cabre, and A. Pascual-Leone, *Noninvasive Human Brain Stimulation.* 2007. **9**(1): p. 527-565.
16. Hallett, M., *Transcranial magnetic stimulation and the human brain.* Nature, 2000. **406**(6792): p. 147-50.
17. Brunoni, A.R., et al., *Clinical research with transcranial direct current*

stimulation (tDCS): challenges and future directions. Brain Stimulation, 2012. **5**(3): p. 175-195.
18. Tufail, Y., et al., *Transcranial Pulsed Ultrasound Stimulates Intact Brain Circuits.* Neuron, 2010. **66**(5): p. 681-694.
19. Tufail, Y., et al., *Ultrasonic neuromodulation by brain stimulation with transcranial ultrasound.* Nat Protoc, 2011. **6**(9): p. 1453-70.
20. King, R.L., J.R. Brown, and K.B. Pauly, *Localization of ultrasound-induced in vivo neurostimulation in the mouse model.* Ultrasound Med Biol, 2014. **40**(7): p. 1512-22.
21. Yoo, S.S., et al., *Non-invasive brain-to-brain interface (BBI): establishing functional links between two brains.* PLoS One, 2013. **8**(4): p. e60410.
22. Min, B.K., et al., *Focused ultrasound-mediated suppression of chemically-induced acute epileptic EEG activity.* BMC Neurosci, 2011. **12**: p. 23.
23. Yoo, S.S., et al., *Focused ultrasound modulates region-specific brain activity.* Neuroimage, 2011. **56**(3): p. 1267-75.
24. Deffieux, T., et al., *Low-intensity focused ultrasound modulates monkey visuomotor behavior.* Curr Biol, 2013. **23**(23): p. 2430-3.
25. Legon, W., et al., *Transcranial focused ultrasound modulates the activity of primary somatosensory cortex in humans.* Nat Neurosci, 2014. **17**(2): p. 322-9.
26. Lee, W., et al., *Simultaneous acoustic stimulation of human primary and secondary somatosensory cortices using transcranial focused ultrasound.* BMC Neuroscience, 2016. **17**.
27. Lee, W., et al., *Transcranial focused ultrasound stimulation of human primary visual cortex.* Sci Rep, 2016. **6**: p. 34026.
28. Rezayat, E. and I.G. Toostani, *A Review on Brain Stimulation Using Low Intensity Focused Ultrasound.* Basic and clinical neuroscience, 2016. **7**(3): p. 187-194.
29. Yao, J. and L.V. Wang, *Photoacoustic Microscopy.* Laser & photonics reviews, 2013. **7**(5): p. 10.1002/lpor.201200060.
30. Xia, J., J. Yao, and L.V. Wang, *Photoacoustic tomography: principles and advances.* Electromagn Waves (Camb), 2014. **147**: p. 1-22.
31. Jiang, Y., et al., *Optoacoustic brain stimulation at submillimeter spatial precision.* Nat Commun, 2020. **11**(1): p. 881.
32. Shi, L.L., et al., *A fiber optoacoustic emitter with controlled ultrasound frequency for cell membrane sonoporation at submillimeter spatial resolution.* Photoacoustics, 2020. **20**.
33. Shi, L., et al., *Non-genetic photoacoustic stimulation of single neurons by a tapered fiber optoacoustic emitter.* Light: Science & Applications, 2021. **10**(1): p. 143.
34. Treeby, B. and B. Cox, *k-Wave: MATLAB toolbox for the simulation and reconstruction of photoacoustic wave fields.* 2010. **Journal of Biomedical Optics**(2): p. 021314.
35. Chang, W.-Y., et al., *Candle soot nanoparticles-polydimethylsiloxane composites for laser ultrasound transducers.* 2015. **107**(16): p. 161903.
36. Li, Y., et al., *Miniature fiber-optic high-intensity focused ultrasound device using a candle soot nanoparticles-polydimethylsiloxane composites-coated photoacoustic lens.* Optics Express, 2018. **26**(17): p. 21700-21711.
37. Lee, W., et al., *Transcranial focused ultrasound stimulation of human primary visual cortex.* Scientific Reports, 2016. **6**(1): p. 34026.
38. Yu, K., et al., *Transcranial Focused Ultrasound Neuromodulation of Voluntary Movement-Related Cortical Activity in Humans.* IEEE transactions on bio-medical engineering, 2021. **68**(6): p. 1923-1931.
39. Yuan, Y., et al., *Cortical Hemodynamic Responses Under Focused Ultrasound Stimulation Using Real-Time Laser Speckle Contrast Imaging.* 2018. **12**(269).
40. Cheng, Z., et al., *High resolution ultrasonic neural modulation observed via in vivo two-photon calcium imaging*. 2021, bioRxiv.

41. Menz, M.D., et al., *Radiation Force as a Physical Mechanism for Ultrasonic Neurostimulation of the Ex Vivo Retina.* 2019. **39**(32): p. 6251-6264.
42. Lockwood, G.R., D.H. Turnbull, and F.S. Foster, *Fabrication of high frequency spherically shaped ceramic transducers.* IEEE Transactions on Ultrasonics, Ferroelectrics, and Frequency Control, 1994. **41**(2): p. 231-235.
43. Baac, H.W., et al., *Carbon-Nanotube Optoacoustic Lens for Focused Ultrasound Generation and High-Precision Targeted Therapy.* Scientific Reports, 2012. **2**(1): p. 989.
44. Chang, W.Y., et al., *Evaluation of Photoacoustic Transduction Efficiency of Candle Soot Nanocomposite Transmitters.* IEEE Transactions on Nanotechnology, 2018. **17**(5): p. 985-993.
45. Chang, W., et al. *Photoacoustic transduction efficiency evaluation of candle soot nanoparticles/PDMS composites*. in *2017 IEEE 17th International Conference on Nanotechnology (IEEE-NANO)*. 2017.
46. Deng, X., et al., *Candle Soot as a Template for a Transparent Robust Superamphiphobic Coating.* 2012. **335**(6064): p. 67-70.
47. Jiang, Y., et al., *Neural Stimulation In Vitro and In Vivo by Photoacoustic Nanotransducers.* Matter, 2021. **4**(2).
48. Gaub, B.M., et al., *Neurons differentiate magnitude and location of mechanical stimuli.* 2020. **117**(2): p. 848-856.
49. Ayling, O.G.S., et al., *Automated light-based mapping of motor cortex by photoactivation of channelrhodopsin-2 transgenic mice.* Nature Methods, 2009. **6**(3): p. 219-224.
50. Malakhova, O.E. and P.W. Davenport, *c-Fos expression in the central nervous system elicited by phrenic nerve stimulation.* J Appl Physiol (1985), 2001. **90**(4): p. 1291-8.
51. Zhong, J., et al., *c-Fos expression in the paternal mouse brain induced by communicative interaction with maternal mates.* Molecular Brain, 2014. **7**(1): p. 66.
52. Beisteiner, R., et al., *Transcranial Pulse Stimulation with Ultrasound in Alzheimer's Disease—A New Navigated Focal Brain Therapy.* 2020. **7**(3): p. 1902583.
53. Tamaddoni, H.A., et al., *Acoustic Methods for Increasing the Cavitation Initiation Pressure Threshold.* IEEE Transactions on Ultrasonics, Ferroelectrics, and Frequency Control, 2018. **65**(11): p. 2012-2019.
54. Bader, K.B., E. Vlaisavljevich, and A.D. Maxwell, *For Whom the Bubble Grows: Physical Principles of Bubble Nucleation and Dynamics in Histotripsy Ultrasound Therapy.* Ultrasound in medicine & biology, 2019. **45**(5): p. 1056-1080.
55. Rabell-Montiel, A., et al., *Acoustic Properties of Small Animal Soft Tissue in the Frequency Range 12-32 MHz.* Ultrasound Med Biol, 2018. **44**(3): p. 702-713.
56. O'Brien, W.D., Jr., et al., *The risk of exposure to diagnostic ultrasound in postnatal subjects: thermal effects.* J Ultrasound Med, 2008. **27**(4): p. 517-35; quiz 537-40.
57. Shapiro, M.G., et al., *Infrared light excites cells by changing their electrical capacitance.* Nature Communications, 2012. **3**(1): p. 736.
58. Braun, V., et al., *Transcranial ultrasound stimulation in humans is associated with an auditory confound that can be effectively masked.* Brain Stimulation, 2020. **13**(6): p. 1527-1534.
59. Sato, T., M.G. Shapiro, and D.Y. Tsao, *Ultrasonic Neuromodulation Causes Widespread Cortical Activation via an Indirect Auditory Mechanism.* Neuron, 2018. **98**(5): p. 1031-1041.e5.
60. Ibsen, S., et al., *Sonogenetics is a non-invasive approach to activating neurons in Caenorhabditis elegans.* Nature Communications, 2015. **6**(1): p. 8264.
61. Krasovitski, B., et al., *Intramembrane cavitation as a unifying mechanism for ultrasound-induced bioeffects.* 2011. **108**(8): p. 3258-3263.
62. Plaksin, M., E. Kimmel, and S. Shoham, *Cell-Type-Selective Effects of*

Intramembrane Cavitation as a Unifying Theoretical Framework for Ultrasonic Neuromodulation. eNeuro, 2016. **3**(3): p. ENEURO.0136-15.2016.

63. Plaksin, M., S. Shoham, and E. Kimmel, *Intramembrane cavitation as a predictive bio-piezoelectric mechanism for ultrasonic brain stimulation.* Physical review X, 2014. **4**(1): p. 011004.
64. Constans, C., et al., *Potential impact of thermal effects during ultrasonic neurostimulation: retrospective numerical estimation of temperature elevation in seven rodent setups.* Physics in Medicine & Biology, 2018. **63**(2): p. 025003.
65. Darrow, D.P., et al., *Reversible neuroinhibition by focused ultrasound is mediated by a thermal mechanism.* Brain stimulation, 2019. **12**(6): p. 1439-1447.
66. Ye, P.P., J.R. Brown, and K.B. Pauly, *Frequency Dependence of Ultrasound Neurostimulation in the Mouse Brain.* Ultrasound in Medicine & Biology, 2016. **42**(7): p. 1512-1530.
67. Fan, H., et al., *Acoustic frequency-dependent physical mechanism of sub-MHz ultrasound neurostimulation.* 2021: p. 2021.09.11.458049.
68. Prieto, M.L., et al., *Dynamic Response of Model Lipid Membranes to Ultrasonic Radiation Force.* PLOS ONE, 2013. **8**(10): p. e77115.
69. Wenger, N., et al., *Spatiotemporal neuromodulation therapies engaging muscle synergies improve motor control after spinal cord injury.* Nature Medicine, 2016. **22**(2): p. 138-145.
70. Zheng, H., et al., *A shape-memory and spiral light-emitting device for precise multisite stimulation of nerve bundles.* Nature Communications, 2019. **10**(1): p. 2790.
71. Maxwell, A.D., et al., *Noninvasive thrombolysis using pulsed ultrasound cavitation therapy - histotripsy.* Ultrasound Med Biol, 2009. **35**(12): p. 1982-94.
72. Kim, J., et al., *Candle Soot Carbon Nanoparticles in Photoacoustics: Advantages and Challenges for Laser Ultrasound Transmitters.* IEEE Nanotechnol Mag, 2019. **13**(3): p. 13-28.
73. Vasan, A., et al., *Microscale Concert Hall Acoustics to Produce Uniform Ultrasound Stimulation for Targeted Sonogenetics in hsTRPA1-Transfected Cells.* Adv. NanoBiomed Res., 2022: p. 2100135.
74. O'Reilly, M.A., Y. Huang, and K. Hynynen, *The impact of standing wave effects on transcranial focused ultrasound disruption of the blood-brain barrier in a rat model.* Phys Med Biol, 2010. **55**(18): p. 5251-67.
75. Azuma, T., et al., *Bubble Generation by Standing Wave in Water Surrounded by Cranium with Transcranial Ultrasonic Beam.* Japanese Journal of Applied Physics, 2005. **44**(6B): p. 4625-4630.
76. Younan, Y., et al., *Influence of the pressure field distribution in transcranial ultrasonic neurostimulation.* Med Phys, 2013. **40**(8): p. 082902.
77. Toda, M. and M. Thompson, *Novel multi-layer polymer-metal structures for use in ultrasonic transducer impedance matching and backing absorber applications.* IEEE Transactions on Ultrasonics, Ferroelectrics, and Frequency Control, 2010. **57**(12): p. 2818-2827.
78. Cannata, J.M., et al. *Design of focused single element (50-100 MHz) transducers using lithium niobate*. in *2000 IEEE Ultrasonics Symposium. Proceedings. An International Symposium (Cat. No.00CH37121)*. 2000.

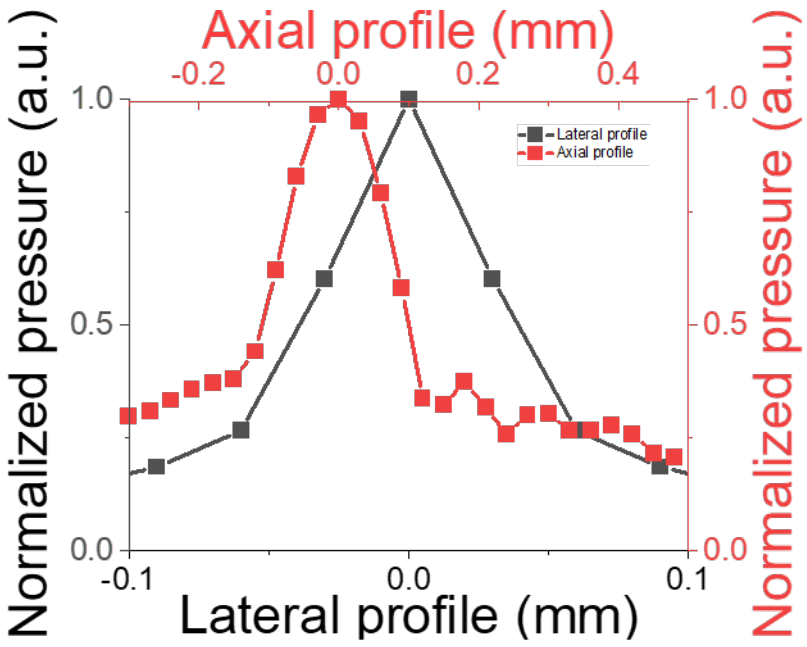

Fig. S1. Lateral and axial profiles of OFUS simulation. The lateral (black) and axial (red) profiles of generated acoustic field was plotted.

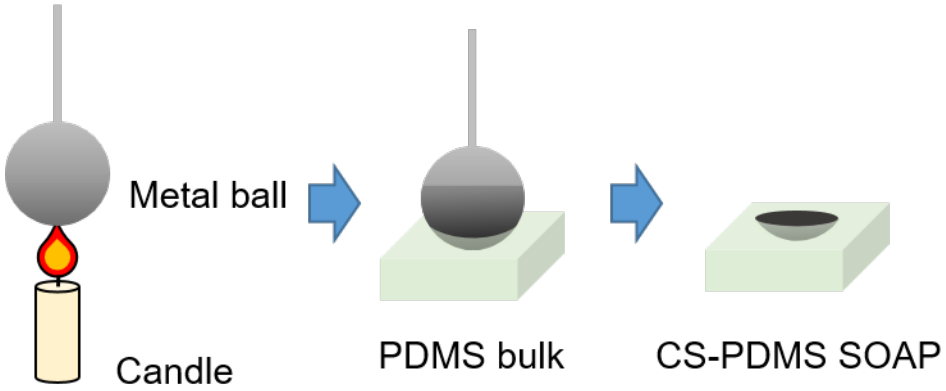

Fig. S2. Fabrication process of CS-PDMS SOAP.

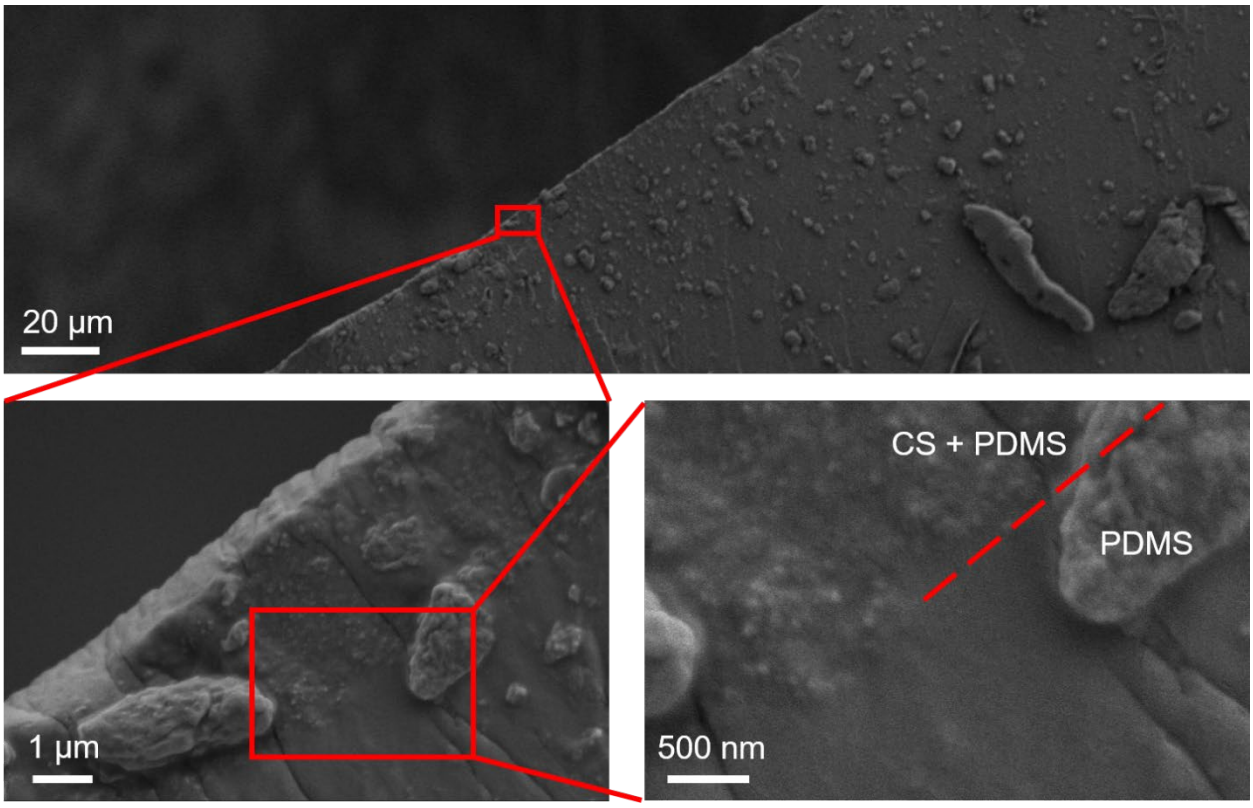

Fig. S3. SEM image of candle soot and PDMS mixture. Dashed red line separated candle soot and PDMS mixture region and pure PDMS region. The mixture region has a rough surface with embedded CS particles. The pure PDMS region has a smooth surface.

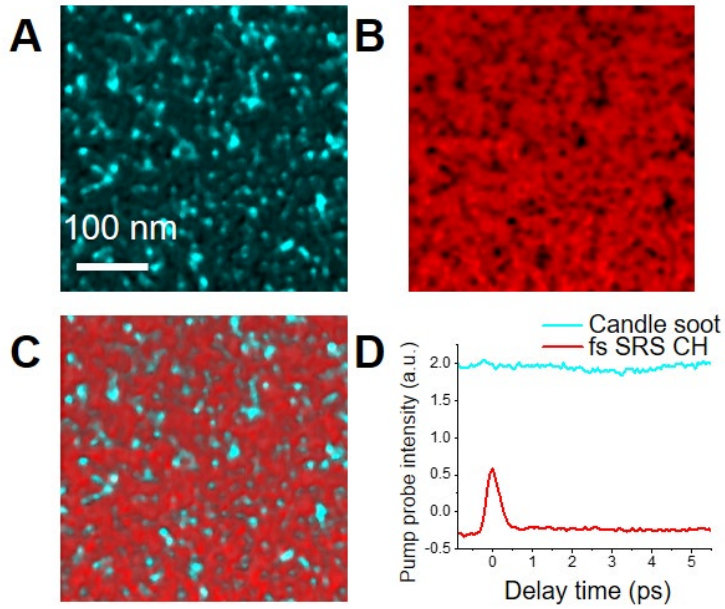

Fig. S4. SRS and photothermal imaging of PDMS and CS in a matrix. (**A**) Photothermal signal from CS reveals its distribution in the CS-PDMS mixture. (**B**) SRS signal from C-H bond in PDMS reveals its distribution in the CS-PDMS mixture. (**C**) Merged composition map of CS-PDMS. (**D**) The pump probe intensity over tuned delay in CS-PDMS mixture. Cyan: the photothermal signal from CS. Red: femtosecond SRS channel for C-H bond signal from PDMS.

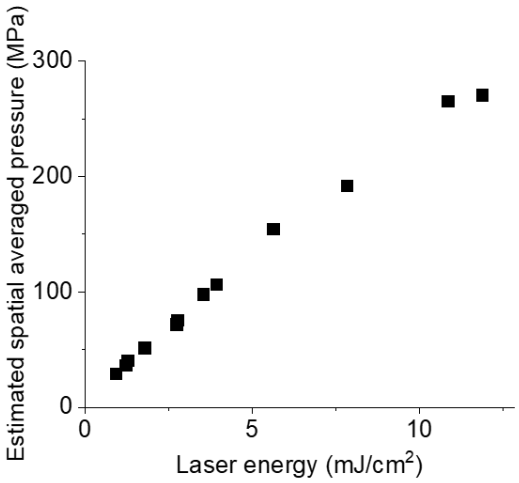

Fig. S5. Ultrasound pressure generated varying input laser pulse energy. Spatial average was taken over an area of 66 × 66 μm^2. The signal below 50 MPa was directly measured by a hydrophone. The signal above 50 MPa was estimated using the method described in the Method session.

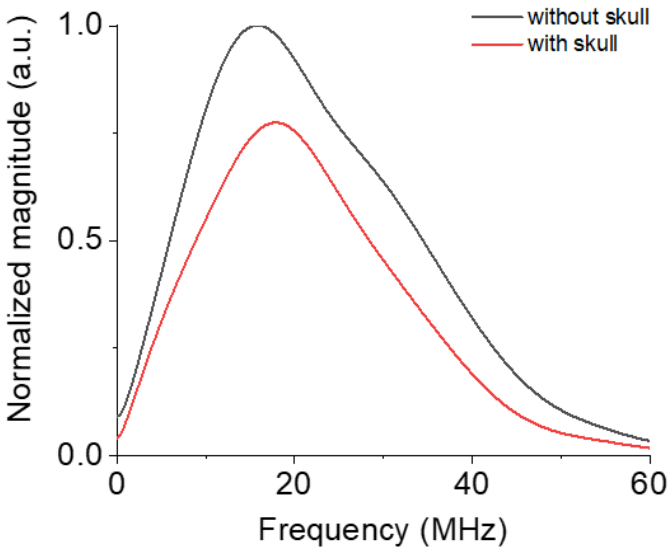

Fig. S6. Frequency spectrum of OFUS without and with a mouse skull. Data were normalized to the peak amplitude of the signal without the presence of the skull at the focus.

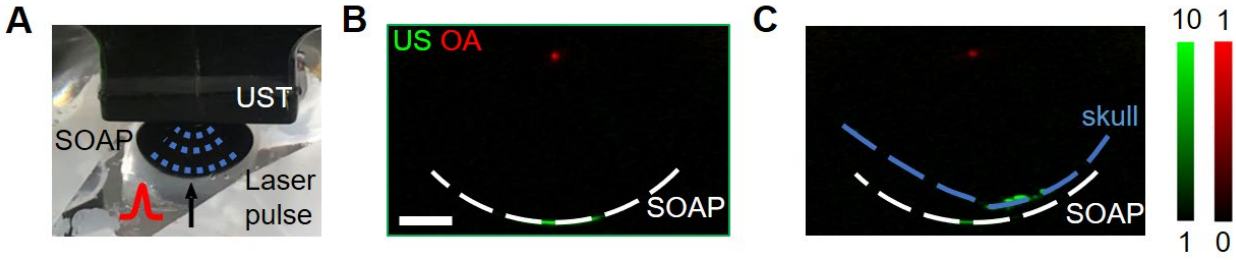

Fig. S7. Visualization of ultrasound propagation with OAT system. (**A**) Photo of OA imaging experimental setup. A pulsed laser (red) illuminated OFUS from bottom and OA signal (blue) was collected by an ultrasound transducer array (UST) from above. (**B, C**) merged image of ultrasound signal (green) and optoacoustic signal (red) without and with mouse skull. Optoacoustic signal is the ultrasound focus that generated by OFUS. White dashed line: OFUS. Blue dashed line: mouse skull. Scale bar: 2 mm.

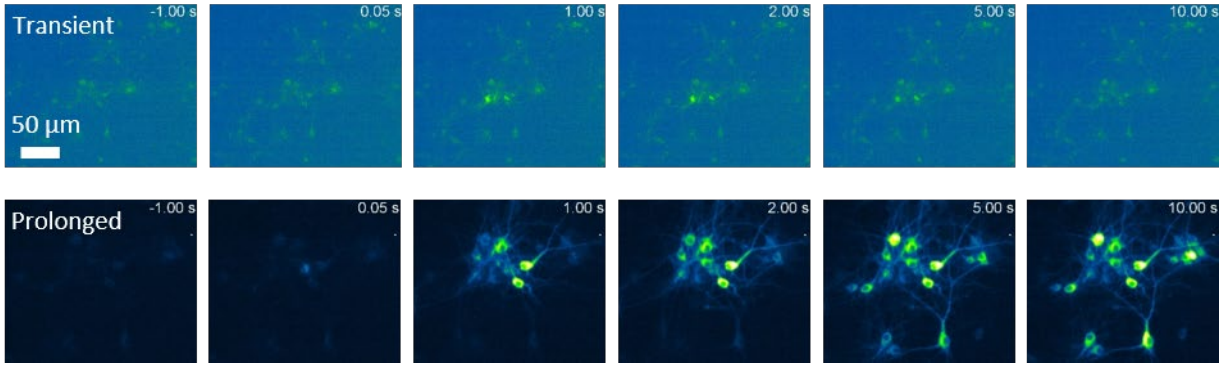

Fig. S8. Representative time lapse images of the transient and prolonged cell response.

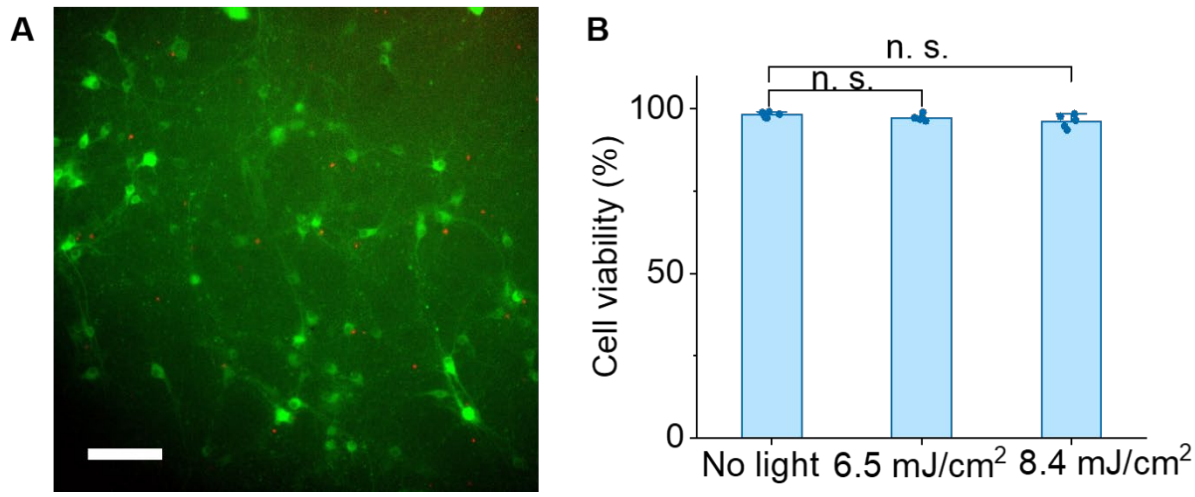

Fig. S9. Viability study of neurons after repeated stimulation. (A) Representative image of live and dead cell staining after repeated stimulation with 5.9 mJ/cm^2 laser input. Scale bar: 100 μm. (**B**) Statistic of cell viability. n.s., not significant ($p > 0.5$).

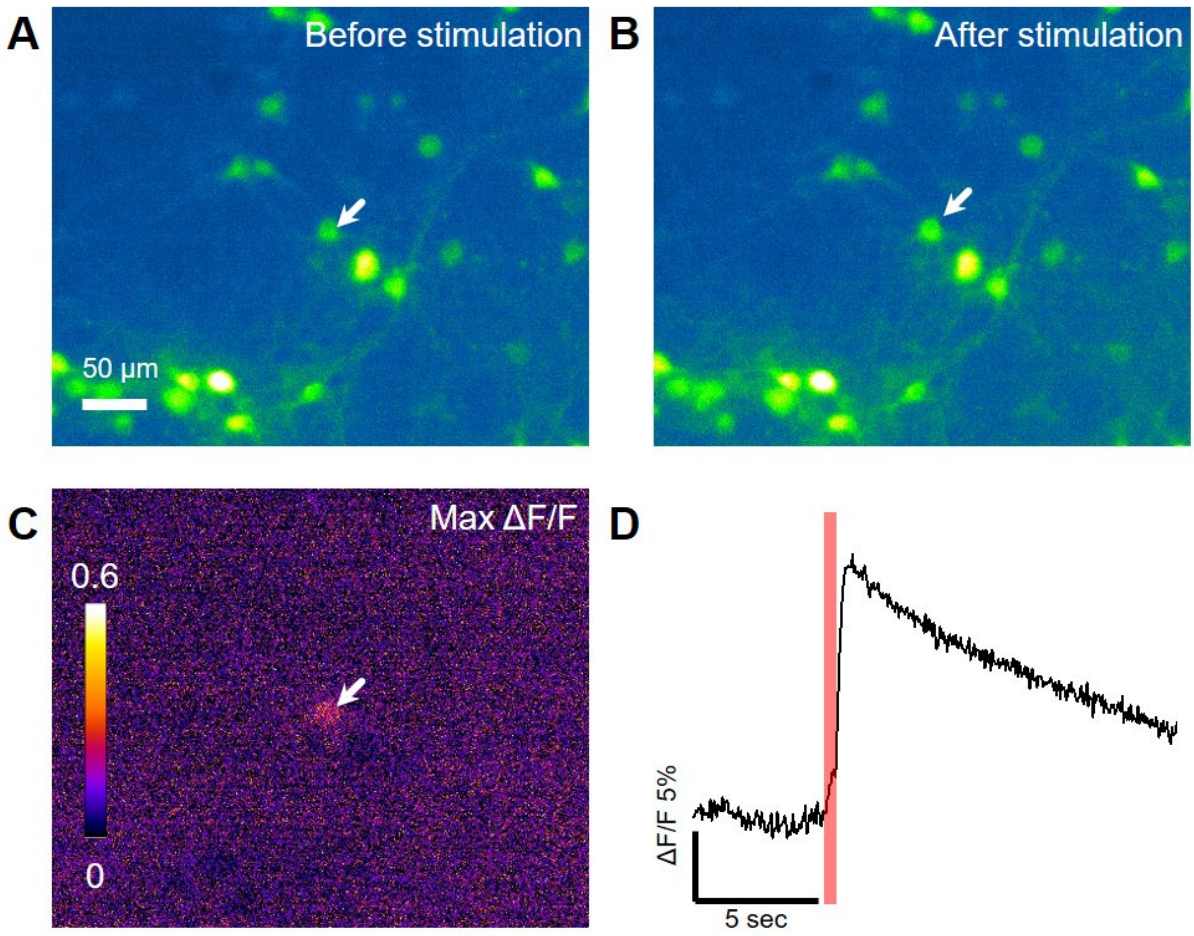

Fig. S10. Neurostimulation with 0.5 MHz focused ultrasound transducer. (**A**) Fluorescence imaging of before and (**B**) after 0.5 MHz focused ultrasound stimulation. (**C**) Max ΔF/F. (**D**) Calcium signal of stimulated neuron.

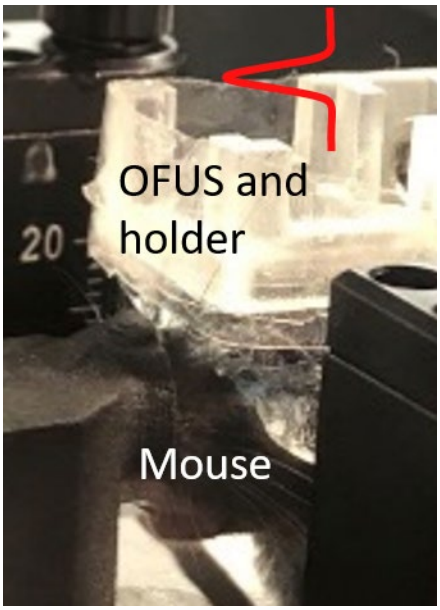

Fig. S11. A photo of experimental setup of OFUS stimulation *in vivo.*

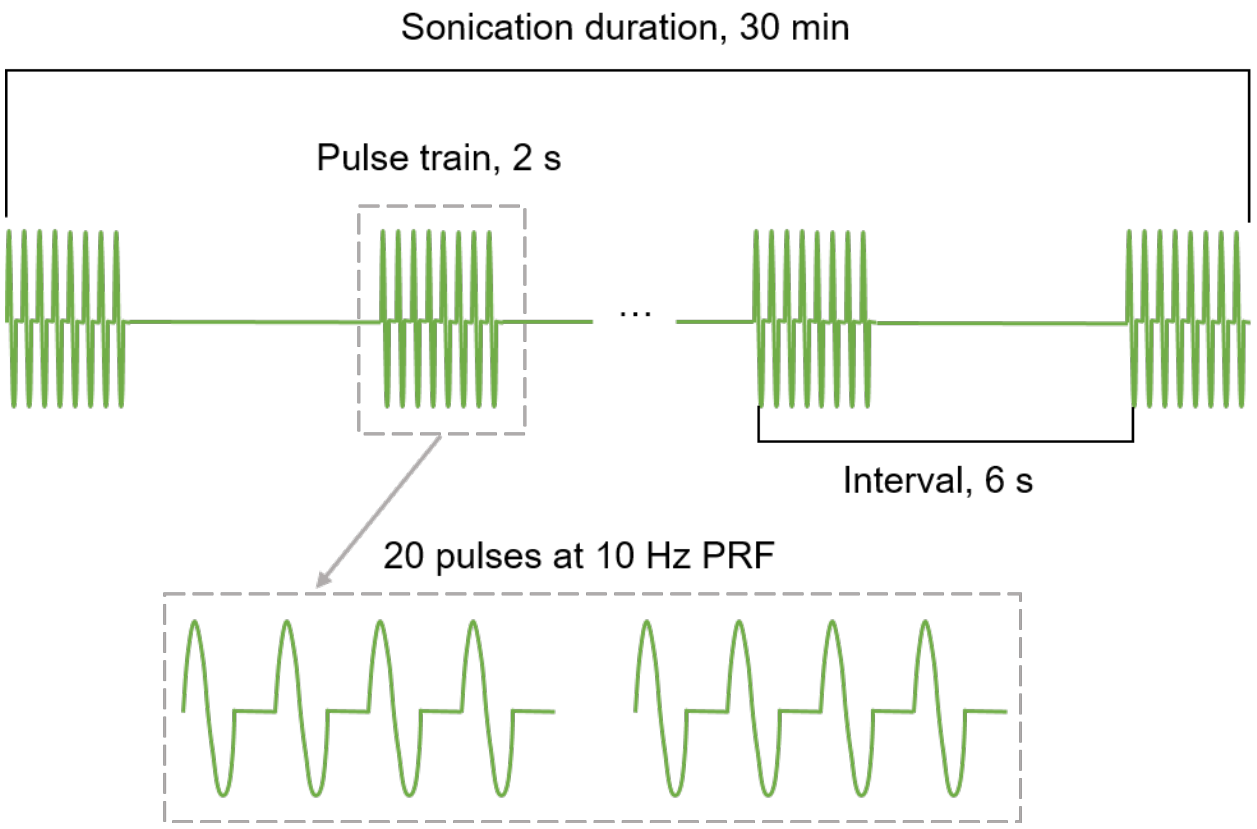

Fig. S12. Ultrasound pulse train diagram for OFUS stimulation to express c-Fos.

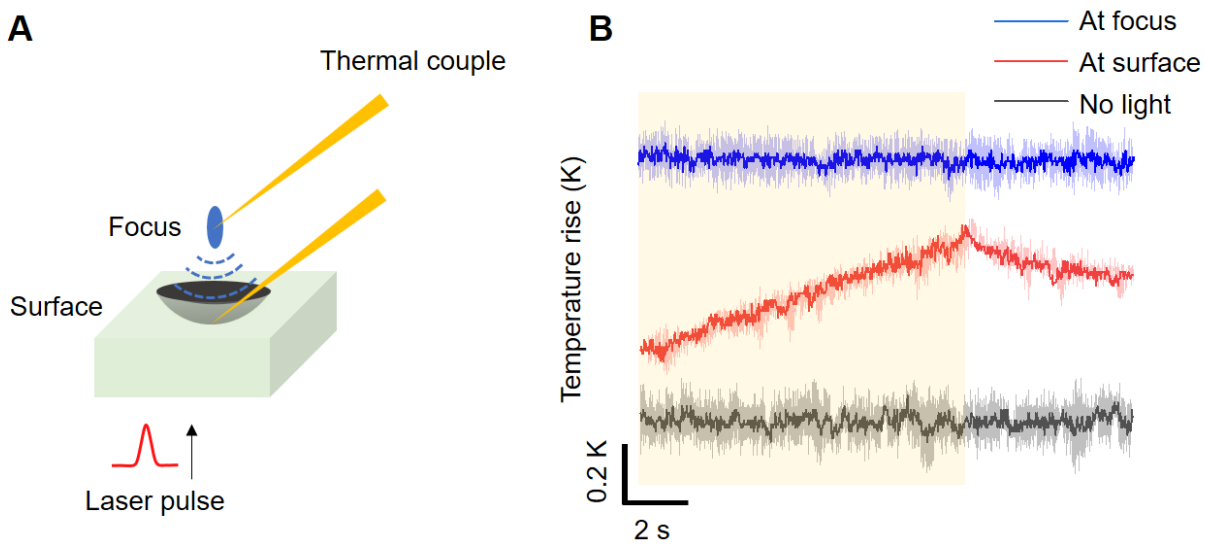

Fig. S13. Temperature profile of OFUS. (**A**) The experimental setup of temperature measurement. (**B**) The temperature profile recorded for 15 s. Yellow box: laser on.